Oncogenic MAPK pathway activation induces a congenital and progressively lethal rare neuropathy in mice

Elise Marechal[1], Daniel Aldea[1,%], Patrice Quintana[1,%,#], Grégoire Mondielli[1], Nathalie Bernard-Marissal[1], Mathias Moreno[1], Claire El Yazidi[1], Natacha Broucqsault[1], Valérie Delague[1], Lauren A. Weiss[2,3], Anne Barlier[1,4], Heather C. Etchevers[1,*]

[1] INSERM, Marseille Medical Genetics, U1251, MarMaRa Institute, Aix Marseille University, Marseille, France
[2] Department of Psychiatry and Behavioral Sciences, University of California, San Francisco, San Francisco, CA 94143, USA
[3] Institute for Human Genetics, University of California, San Francisco, San Francisco, CA 94143, USA
[4] AP-HM, MMG, MarMaRa Institute, La Conception Hospital Laboratory of Molecular Biology, Marseille, France.

% These authors have contributed equally to this work.

[#] Current address: University of Clermont Auvergne, INSERM, U1107, NEURO-DOL, Clermont-Ferrand, France

[*] Corresponding author

E-mail : heather.etchevers@inserm.fr

Short title: Sustained Braf promotes cellular immaturity

Keywords: rare disease, mosaicism, signaling, neural crest, glia, cancer, development

Abstract

RASopathies, rare congenital syndromes affecting skin, heart, brain and skeletal systems, often include peripheral neuropathy of unknown origin. Although RASopathy gene variants are familiar proto-oncogenes after birth, the causal relationships between timing and specific pathological outcomes remain unclear. This study examined how a mitogen-activated protein kinase (MAPK) effector, Braf, causes peripheral neuropathy. Targeting the oncogenic Braf(V600E) variant, found in mosaic RASopathies, to cells having expressed myelin protein zero (Mpz) in mice triggered a degenerative neuropathy evoking type 1 Charcot-Marie-Tooth syndrome, with pre-weaning onset of hyperplastic nerves, hindlimb weakness, and unexpectedly reduced body size. Constitutively active Braf expanded a Jun+ Schwann cell repair state, impairing myelination by mature Schwann cells. Patient-derived iPSCs bearing the *BRAF* Q257R variant, associated with cardio-facio-cutaneous syndrome, failed to differentiate into mature Schwann cells, instead exhibiting transcriptional profiles associated with progenitor or repair states. These findings suggest that somatic mosaicism may contribute to unresolved genetic heterogeneity in human neuropathies and enlarge the candidate gene list. They also reveal a MAPK-dependent mechanism by which neural crest-derived Schwann cells regulate both body growth and peripheral nerve homeostasis.

Introduction

Many cancers and congenital diseases co-opt and deploy the molecular mechanisms of normal organogenesis in inappropriate contexts. Activation of the mitogen-activated protein kinase (MAPK) intracellular signaling pathway drives dozens of solid and liquid cancers in somatic tissues of humans and animal models [1]. In contrast, RASopathies are heterogeneous developmental syndromes that preferentially affect epidermis and pigmentation; cardiovascular, craniofacial and skeletal systems; and neurological or endocrine functions impacting body size and fertility [2–7]. Variants of at least 24 genes that boost and sustain MAPK signaling to, and nuclear translocation of, the extracellular signal-regulated kinases (ERK1/2) are responsible for pathogenesis [8]. Activating variants may be expressed constitutionally or prenatally restricted to yield lineage-specific mosaic or somatic RASopathies [9]. Most RASopathies are associated with specific cancer predispositions in constitutional and somatic presentations, particularly when syndromic [10,11].

A limited number of specific MAPK pathway variants engender this wide spectrum of overlapping clinical outcomes. Oncogenic variants in *BRAF*, particularly encoding changes to valine (p.V)600, drive aggressive forms of melanoma as well as thyroid, colorectal, lung, ovarian and breast cancers [1,12–14]. BRAF p.V600E has never been observed in germline disease because of early embryonic lethality, observed in mouse models [15], and cellular cytotoxicity through its strong constitutive ERK1/2 activation. BRAF p.V600E yields an active, monomeric kinase, independent of RAS-mediated transduction [16,17]. In contrast, mild pathway-activating *BRAF* variants such as p.Q257R underlie a growing list of congenital RASopathies [10,18–20]. These include the germline RASopathies, cardio-facio-cutaneous syndrome (CFC; ORPHA:1340) and Noonan syndrome with (ORPHA:500) or without (ORPHA:648) multiple lentigines. Their common clinical features include reduced postnatal growth, dysmorphic facial features, melanocytic nevi or other pigmented lesions, congenital heart defects, and tumor predispositions [21–24].

The mechanisms and triggers of neuropathies in the context of RASopathies have not been explored to date. Only recently have multiple CFC and Noonan syndrome patients been reported with neuropathies causing pain, sensory loss and/or muscle wasting [25–27], evoking similar symptoms in Charcot-Marie-Tooth syndrome, type 1 (CMT1; Callegari et al., 2019). *Mek1*, the major MAP kinase kinase (MAP2K) phosphorylating Erk1/2, is known to be necessary for nerve myelination during maturation, while its conditional over-expression or sustained activity in mature Schwann cells (SC; peripheral glia) induces murine neuropathy [29–32]. Although CMT is genetically heterogeneous, with many dozens of causal genes identified,

none are known MAPK effector genes; that said, one in six clinical CMT1 patients still do not have a molecular diagnosis [33].

Human peripheral nervous system (PNS) architecture and conduction depend fully on SC, which provide physical and trophic nerve support while myelinating large, fast-conduction axons [34–36]. The entire PNS, including SC and perineurial stroma of its sensory and autonomic components, derives from the multipotent embryonic neural crest (NC) population, which also supplies critical craniofacial and cardiovascular connective tissues and all melanocytes [36,37]. Given the shared origin of numerous cell types affected in germline RASopathies, we hypothesized that multipotent NC-derived lineages may be particularly vulnerable to increased MAPK signaling before birth. The ability of NC-derived cells to instruct fate or regulate homeostasis in neighboring tissues over time may also be compromised.

The goal of this study was to assess systemic and cell-autonomous effects of constitutively active BRAF signaling on multipotent, NC-derived progenitor differentiation. We found that conditional expression of *Braf* p.V600E in mouse cells having expressed the SC-specific gene *Mpz* (encoding myelin protein zero, or P0) led to a peripheral neuropathy in association with induction and maintenance of an ineffective repair SC phenotype. Although nerve myelination initiated after birth as usual, mutant peripheral glia rapidly misregulated hundreds of genes associated with mature SC function, including myelination, and nerves underwent active myelin destruction. Unexpectedly, although endocrine tissues had not been intentionally targeted in this model, mice also underwent developmental delay and remained sexually ambiguous or immature. Furthermore, human pluripotent cells derived from two teenaged donors with CFC syndrome, carrying the most frequent postnatal activating *BRAF* missense variant, p.Q257R, were also incapable of terminal SC differentiation *in vitro*, in contrast to cells from wildtype donors, after upregulating repair SC transcripts. Our results suggest that molecularly undiagnosed cases of RASopathies, or endophenotypes such as CMT type 1 or idiopathic cryptorchidism [38], may be imputable to somatic mosaicism for oncogenic MAPK pathway gene variants in the NC lineage.

Results

Sustained Schwann cell MAPK signaling in causes juvenile locomotor and growth deficits

In order to model constitutive Braf-mediated signaling in progenitors of Schwann cells *in vivo*, we used *Mpz-Cre*$^{+/°}$ mice, which transcribe *Mpz* (encoding myelin protein zero, or P0) as early as embryonic day 12 in neural crest cells [39,40]. Crossed to a knock-in floxed *Braf* allele bearing the hotspot V600E variant (*Braf*^{V600E}) (**Fig S1a**), the *Mpz-Cre*$^{+/°}$;*Braf*$^{V600E/+}$ mice, abbreviated hereafter as Mpz-*Braf*, were born at expected Mendelian ratios and remained asymptomatic

114 for the first week. However, from postnatal day (P)7, all Mpz-*Braf* mutants developed signs of
115 peripheral neuropathy including tremors, abnormal hindlimb postural reflexes and trailing legs
116 (**Fig 1a**). They nonetheless showed age-appropriate activity in exploration, feeding and
117 grooming. Correlating with phenotypic onset, mutant sciatic nerves exhibited significantly more
118 Erk1/2 phosphorylation than controls, increasing from early (P5; **Fig 1c, e**) to later (P21; **Fig**
119 **1d, e**) stages of SC-mediated myelination, demonstrating congenital and persistent MAPK
120 activation in peripheral glia.

121 After P10, mutant mice were also visibly smaller than control littermates, with significantly
122 reduced but proportional nose-to-tail length and weight (**Fig 1f**). Proportionately small body
123 size could result from a deficiency in growth hormone (Gh), particularly as activating *BRAF*
124 mutations have been described in the context of human hypopituitarism [2]. To see whether
125 there were any changes in hormonal transcription, pituitaries at P5 were compared between
126 control and Mpz-*Braf* mice by bulk RNA-sequencing (RNAseq). As for all other genes, Gh
127 releasing hormone receptor *Ghrhr* or *Gh* transcripts, were not significantly altered in the two
128 groups at this stage (**Fig S1b**; **Table S1**). Gh binds to peripheral Ghr, a type I cytokine receptor,
129 to regulate the production of its effector insulin-like growth factor 1 (Igf1) in the liver and other
130 sites, exerting thereby anabolic effects on bone and muscle [41]. We therefore compared the
131 transcription of *Ghr* and *Igf1* by RT-qPCR in the livers of P21 Mpz-*Braf* and control littermate
132 mice. While *Ghr* was upregulated on average by 3.3-fold in mutant livers, Igf1 was far more
133 significantly diminished, by 211-fold (**Fig 1g**). The juvenile Mpz-*Braf* growth anomaly was the
134 likely consequence of a near-complete loss of peripheral Igf1 production.

135 *Braf*$^{V600E/+}$ in SCs induces widespread peripheral nerve demyelination and axonal loss

136 Strikingly broad nerves were visible in all Mpz-*Braf* mice upon autopsy at P5 or P21; mutant
137 nerves also lacked structural bands of Fontana [42] (**Fig 2a**; **Fig S1**). Despite their smaller
138 bodies, Mpz-*Braf* sciatic nerves were significantly wider at P10 (0.48 ± 0.07 *vs* 0.31 ± 0.05 mm
139 diameter in controls; **Fig 2b**). This discrepancy stabilized after weaning (0.74 ± 0.09 *vs* 0.39 ±
140 0.05 mm at P21, and 0.78 ± 0.05 *vs* 0.50 ± 0.04 mm at P35, respectively). Similar enlargement
141 was also evident in all other peripheral nerves of Mpz-*Braf* mice examined at P21, including
142 the sensorimotor peroneal, tibial, sural, trigeminal and ophthalmic nerves and the sensory
143 saphenous and maxillary nerves (**Fig S1c-e**).

144 To further evaluate myelination dynamics and study the ultrastructural composition of mutant
145 sciatic nerves, we used transmission electron microscopy (EM) to study cross-sections at P5,
146 P21 and P28. Over time, degenerating axons, extracellular collagen, fibroblasts, macrophages
147 and numerous SC nuclei could be identified. Myelin aberrations were frequent in Mpz-*Braf*
148 nerves from P21 on, including examples of tomaculae, infoldings, onion bulbs and

149 degenerated axons, and focal hypermyelination of small-caliber axons, among other
150 anomalies (**Fig 2c**; **Fig S2a-d**). These structures were interspersed with abundant extracellular
151 collagen fibrils and tentacular fibroblasts (**Fig 2c**) and, by P42, axon-associated macrophages
152 containing myelin debris (**Fig S2e-f**). In contrast, at P5, no significant differences were
153 observed in average axonal density (52 ± 2 axons/mm^2 in Mpz-*Braf* *vs* 48 ± 3 axons/mm^2 in
154 controls) or diameter (1.447 ± 0.026 µm in Mpz-*Braf* *vs* 1.476 ± 0.072 µm in controls; **Fig 3a**;
155 **Fig S3a-b**). Likewise, no differences in immune infiltration were observed, while myelin
156 thickness as quantified by the *g*-ratio, the ratio of inner to outer diameters of axonal myelin
157 sheaths [43], remained constant (**Fig 3b** and **Fig S3c-d**) at an average of 0.732 ± 0.019 in Mpz-
158 *Braf* vs 0.708 ± 0.028 in controls. Only occasional myelin aberrations were observed in mutant
159 nerve cross-sections at this early stage (**Fig 2c**). Radial sorting and myelination therefore
160 began similarly in mutant and control peripheral nerves.

161 In contrast, axon density by P21 had declined significantly more in Mpz-*Braf* mutants than age-
162 matched controls (respectively, 4,060 ± 1,378 axons/mm^2 *vs* 36,172 ± 2,726 axons/mm^2; **Fig**
163 **3c**). By P28, a mean 7.2% of myelinated axons persisted in mutant sciatic nerves (1,841 ± 465
164 axons/mm^2 *vs* 25,703 ± 2,812 axons/mm^2 in controls; **Fig 3c**). Residual mutant axons were
165 significantly smaller on average (**Fig 3d-e**; 1.89 ± 0.23 µm in Mpz-*Braf* vs 2.64 ± 0.07 µm in
166 controls). To see which calibers of axons were affected, we examined width distributions of
167 792 and 746 myelinated axons at P28 from mutant and control mice, respectively (**Fig 3f**).
168 After weaning, there was relative loss of large axons of over 3 µm in diameter (**Fig 3e-f; Fig**
169 **S3e**; on average: 8.7 ± 6.7% in Mpz-*Braf* vs 33.3 ± 5.6% in controls).

170 The residual axons displayed 12% higher *g*-ratios, indicating thinner average myelin sheaths
171 (**Fig 3f; Fig S3f**; *g*-ratios: 0.66 ± 0.02 in Mpz-*Braf* vs 0.59 ± 0.00 in controls). To see if all axons
172 were affected equally, results were binned into small (<1 µm), medium (1-3 µm) and large (3
173 µm) diameter axons. Medium- and large-caliber axons had significantly thinner myelin in
174 mutants compared to controls (**Fig 3g**; average *g*-ratios: 0.67 ± 0.03 *vs* 0.59 ± 0.01 for medium-
175 caliber axons; 0.75 ± 0.00 *vs* 0.60 ± 0.01 for large-caliber axons). In contrast, small-caliber
176 axons exhibited a modest (10.6%) but significant increase in myelination (*g*-ratios of 0.47 ±
177 0.01 in mutants *vs* 0.52 ± 0.02 in controls; *cf*. **Fig 2c**, **Fig S2d**). In control mice, myelin thickness
178 increases with axon caliber to plateau at 4 µm and greater [30]. Fast-conduction axons of
179 motoneurons [44] were thus most severely affected in terms of myelination and persistence,
180 while some smaller axons were subject to hypermyelination.

181 Myelin component mislocalization and SC progenitor expansion

182 Extending these structural findings, we examined distribution of components of the myelinated
183 axon by teasing apart fixed fibers from P5 and P21 sciatic nerves. Immunofluorescence against

184 contactin-associated protein 1 (Caspr, also called paranodin) demonstrated that in contrast to
185 controls (**Fig 4a**), residual myelin internodes were irregularly spaced, diffuse or absent along
186 mutant axons (**Fig 4b, d-g**). Early breakdown of myelin during its establishment in neighboring
187 axons was already visible in longitudinal view at P5, when F-actin labeling highlighted
188 successive beads of myelin ovoids along some mutant sciatic fibers (**Fig 4b-d**). By P21 (**Fig**
189 **4e**), only Mpz-*Braf* mice displayed some demyelinated segments entirely devoid of myelin
190 basic protein (Mbp) along individual fibers (**Fig 4f**). Multiple adherent nuclei between residual
191 Caspr+ nodes (**Fig 4f**), instead of a single SC following normal radial sorting [45], are consistent
192 with persistence of immature Mpz-*Braf* SCs.

193 To visualize SCs capable of proliferating, we examined the expression *in situ* of Sox10 (SRY-
194 box transcription factor 10), present throughout the Schwann cell lifespan [46], and Ki67, a
195 common indicator of cell cycle progression beyond quiescence [47,48], using co-immunostaining
196 of whole sciatic nerves at P42 in sagittal section. While Sox10^{+} nuclei were visible throughout
197 control nerves, with concomitant Ki67 immunofluoresence (**Fig S4a**), double-positive as well
198 as unlabeled nuclei were more densely and haphazardly arranged in the hyperplastic Mpz-
199 *Braf* nerves (**Fig. S4b**). All Sox10^{+} nuclei observed were also strongly Ki67^{+} in mutant nerves,
200 interspersed with additional Ki67^{+} Sox10^{-} cells. Mutant sciatic nerves thus show prolonged
201 hyperplasia rather than hypertrophy, imputable both to probable inflammation and fibrosis but
202 also to sustained SC proliferation.

203 *Braf*$^{V600E/+}$ glia *in vivo* downregulate myelin sheath gene transcription

204 Bulk RNAseq was undertaken to identify global transcriptional changes associated with loss
205 of myelin after MAPK pathway activation, comparing Mpz-*Braf* and control sciatic nerves
206 dissected from four mice at ages P5 and P21 (**Fig 5** and **Table S2**). In contrast to P5 pituitaries,
207 we identified 2,540 differentially expressed genes (DEGs) between P5 mutant and control
208 nerves (*p*adj < 0.05 for significance). By P21, 10,409 DEGs were identified (**Fig 5a**).
209 Constitutive MAPK signaling therefore leads to early, large-scale transcriptional changes in
210 cells composing the sciatic nerves.

211 The myelin sheath consists of 70% to 85% lipids and 15 to 30% proteins [49]. By P21, there was
212 significant downregulation of terms related to cholesterol biosynthesis and metabolism in *Braf*-
213 mutant sciatic nerves (**Fig 5b, c**). However, the annotation "spinal cord injury" was significantly
214 enriched at both P5 and P21 (**Fig 5b**). Among strongly downregulated genes at P21 were
215 *Hmgcr* (11.5-fold), encoding a rate-limiting enzyme in cholesterol biosynthesis [50], and *Fa2h*
216 (7.9-fold), encoding fatty acid 2-hydroxylase, a rate-limiting myelin glycosphingolipid synthesis
217 enzyme [51] (**Table S2**). While *Pmp2* (encoding a fatty acid-binding protein, also called *Fabp8*)

218 and *Omg* (oligodendrocyte myelin glycoprotein) mRNA levels were significantly upregulated in
219 P5 Mpz-*Braf* sciatic nerves, by P21 they were not significantly different from controls (**Fig 5d**).

220 Transcription of other abundant myelin proteins encoded by *Mpz*, *Pmp22* (peripheral myelin
221 protein 22*)* or *Mbp* (myelin basic protein) were not significantly altered at P5, but other myelin
222 components were already significantly if modestly reduced, including transcripts for myelin and
223 lymphocyte protein (*Mal*), periaxin (*Prx*), the myelin-associated 2',3'-cyclic nucleotide 3'
224 phosphodiesterase (*Cnp*), myelin-associated glycoprotein (*Mag*), plasmolipin (*Pllp*) and others
225 **(Fig 5d**; **Table S1**). By P21, when sciatic myelination is nearly complete in controls (**Fig 2**),
226 *Mpz*, *Mbp* and *Pmp22* transcripts among others were significantly less expressed than in
227 controls (**Fig 5d**). The observed demyelination and axonal degeneration phenotype in
228 response to sustained MAPK signaling was a thus a result of transcriptional downregulation of
229 myelin components preceding axonal loss.

230 Transcriptional control of myelination is disrupted by constitutive MAPK signaling

231 We next examined the modulation of transcription factors (TF) that covaried with those known
232 to impact the process of myelination. At P5, the major transcriptional activators *Egr2* (early
233 growth factor response 2, also called Krox20 [52]), and *Sox10* [53], were unaffected. However, by
234 P21, mutant SCs showed a significant decrease in *Egr2* expression with concomitant ectopic
235 increases in neural crest or multipotency maintenance factors *Sox2, Foxd3*, *Tfap2a* and
236 *Tfap2b,* and a significant decrease in the melanocyte determinant *Mitf*, with no effect on *Sox10*
237 transcription (**Fig 6a**; **Table S2**). Simultaneously, SC-associated transcriptional repressors of
238 myelination [54] were significantly upregulated in mutant sciatic nerves at P21, including *Jun*,
239 *Egr1*, *Egr3,* and *Zeb2* (**Fig 6a**). The increase in *Jun* translated into significantly more Jun
240 protein in mutant than control nerves after P21, while the reduction in Egr2 protein was only
241 measurable at P42 (**Fig 6b**).

242 To corroborate the effects of decreased *Egr2* expression in mutant SCs, we reasoned that a
243 distinct model of hypomyelinating neuropathy triggered by germline expression of a
244 homozygous, hypomorphic *Egr2* allele (Le et al., 2005) should show similar transcriptional
245 deregulation. Indeed, GSEA analysis found that the co-variance of 99/110 (90%) significantly
246 increased or 98/107 (91.5%) decreased DEGs between the two animal models itself showed
247 significant correlation (**Fig 6c**; $p < 0.001$). Sciatic nerve hypomyelination is therefore
248 associated with overexpression of Jun and effected by less *Egr2*-driven target transcription.

249 During remyelination after mouse sciatic nerve injury, axonal Nrg1 type III stimulates SC *Pmp2*
250 expression facilitate fatty acid uptake and increase mitochondrial ATP production [55]. We had
251 observed significant *Pmp2* and massive *Nrg1* overexpression in the Mpz-*Braf* RNAseq results
252 (**Table S2**); the major source of Nrg1 after P5 in this model is the SC rather than the axon itself

253 [56]. This reactive overexpression to injury has been shown to be responsible for "onion bulb"
254 formation around neuropathic axons and an ultimately detrimental response to chronic repair
255 SC stimulation [57].

256 Normally, Nrg1-III binds SC-specific ErbB3 to activate MAPK signaling, among other
257 pathways. We hypothesized that the Mpz-*Braf* sciatic nerves at P5 and P21 should show a
258 similar transcriptional response to an *Egr2*-driven gain-of-function *Mek1*DD allele at P8 and
259 P30, which leads to hypermyelination in bypassing the natural decrease of Erbb3 in maturing
260 SC [30]. As *Mek1* functions downstream of *Braf*, there was indeed robust positive correlation (p
261 < 0.0001) at both stages of myelination and significant upregulation of *Erbb3* between P5 and
262 P21 **(Fig 6d**; **Table S2)**. *Egr2*-Cre-driven depletion of the upstream MAPK pathway
263 phosphatase Shp2 entails, instead, a hypomyelinating neuropathy [30]. Shp2 is encoded by
264 *Ptpn11*, a RASopathy gene responsible for Noonan syndrome [58]. We observed significant anti-
265 correlation of DEG between Mpz-*Braf* and *Egr2*^{Cre};*Shp2*$^{f/f}$ sciatic transcriptomes at initial
266 myelinization (P5 vs P8), which changes to positive correlation after weaning (P21 vs P30; **Fig**
267 **6e**).

268 Finally, to see if the PNS effects of oncogenic Braf could be recapitulated by *Egr2*-expressing,
269 rather than *Mpz*-expressing SC *in vivo*, we crossed heterozygous LSL-*Braf*$^{V600E/+}$ mice to the
270 same *Egr2*-Cre driver mice. The *Egr2*-Cre allele is expressed by SCs from mid-gestation on
271 (Topilko et al., 1994; **Fig S5A**). However, mutant neonates were never obtained from this
272 breeding, a significant ($p < 10^{-6}$) departure from the expected yield. Broader expression of *Egr2*
273 in other cell types as compared to *Mpz* prevented further comparisons of postnatal myelination
274 processes, due to fully penetrant embryonic lethality (**Fig S5B**).

275 Uninjured sciatic nerves initiate and sustain an early repair program

276 Transcripts significantly overexpressed at P5 and sustained through P21 in mutant sciatic
277 nerves may reflect direct rather than indirect effects of MAPK signaling. We therefore examined
278 the 175 genes that were significantly upregulated by two-fold or more at both stages with
279 annotations from Wikipathways, KEGG and REACTOME (**Fig S6a**) and GSEA (**Fig S6b**; **Fig.**
280 **7a**). The term "spinal cord injury" (WP2431) remained one of the most significantly enriched
281 even in this subset (cf. **Fig 5b**). In particular, cell adhesion molecule L1 (*Chl1*), one of the most
282 specific transcripts for repair-type SC identified in single-cell RNAseq [34], was highly enriched
283 over time. Comparing the overall transcriptome of Mpz-*Braf* sciatic nerves with that of a 6- to
284 8-week mouse model of axotomy at seven days post-injury [59] showed a significant positive
285 correlation at P5 (**Fig S6c**) that increased with time (**Fig 7b**). The general molecular response
286 to nerve injury is thus active during physiological myelinogenesis in juvenile Mpz-*Braf* mice.

287 Following physical injury such as crush or axotomy, SCs undergo extensive reprogramming,
288 re-expressing genes from less differentiated stages and transcribing novel repair-associated
289 genes. Such transcripts are normally either absent or transcribed at low basal levels in both
290 immature and mature SC. For example, the transcription factor Jun was significantly
291 transcribed and translated at P21 in the Mpz-*Braf* sciatic nerve (**Fig 6a-b**). Jun distinguishes
292 repair SCs in injured adult nerves from immature SCs and represses myelination by opposing
293 Egr2 [60].

294 We next sought to find out if secreted ligands specific to the repair phenotype, described as
295 Jun-dependent, were also strongly upregulated in Mpz-*Braf* sciatic nerves. As early as P5, *Shh*
296 (Sonic hedgehog) and the neurotrophic factor *Gdnf* (glial cell line-derived neurotrophic factor)
297 [61] were significantly upregulated (**Fig 7c**). Cleaved Shh protein is important for multipotent NC
298 maintenance [62] and its precursor is transcribed again in repair SCs upon nerve injury [63]. We
299 confirmed by immunolabeling of fiber bundles (**Fig 7d**) and Western blot **(Fig. 7e**; **Fig S7e**)
300 that Shh and S100b, a calcium-binding intermediate filament common to SCP and their
301 derivatives, [64], were co-localized and significantly more expressed by P21 in Mpz-*Braf* mutant
302 sciatic nerves than control nerves**.**

303 Nrg1-III and the Gdnf family member Artemin (Artn) are also secreted by Jun-positive repair
304 SCs after injury to promote axon outgrowth [56,65]. While *Nrg1* was strongly upregulated at P5
305 and P21, *Artn* was only significantly overexpressed at P21 (**Fig. 7c**). An increase in
306 transcription of the Nrg1 receptor *ErbB3*, a hallmark of nerve damage [66], was translated into
307 significantly more protein at P21 and P42 (**Fig 7c, f-g**; **Fig S7b**). More Erbb3 protein
308 immunofluorescence was also observed in mutant than control nerves, complementary to the
309 Pmp2-positive myelin in individual cells (**Fig. 7f**; **Fig S7d**). We also found increased relative
310 levels of the intermediate filament vimentin, encoded by *Vim*, over time in mutant sciatic
311 nerves, phenocopying the local translation demonstrated in experimentally injured axons
312 [67](**Fig. S7c; Table S2**). Despite heightened expression of repair program genes in Mpz-*Braf*
313 sciatic nerves, pronounced axonal degeneration over time demonstrated that sustained MAPK
314 signaling in SC was counterproductive *in vivo*.

315 Schwann cell differentiation of CFC patient-derived hiPSCs is impaired

316 The Mpz-*Braf* model allowed us to assess some direct molecular consequences of constitutive
317 MAPK signaling on SC biology *in vivo*. However, *BRAF*^{V600E} is not viable in the human (or
318 mouse) germline. In order to assess the effects on SC of the heterozygous activating
319 *BRAF*^{Q257R} variant frequently found in CFC patients, but without the severe cardiac defects
320 preventing postnatal study of existing CFC mouse models [68,69], we differentiated hiPSC lines
321 from two unrelated CFC patients [70] into SC *in vitro* and compared their maturation with that of

322 two unrelated control hiPSC lines. Cells of the control lines were morphologically similar to
323 each other and to the original publication throughout the directed differentiation protocol [71].
324 However, one of the mutant cell lines (RMK0138C) required more frequent passages to
325 maintain a similar density and failed to develop the elongated, refringent soma and long
326 projections characteristic of SCPs in the three other lines, even after 90 days *in vitro* and
327 despite the same *BRAF* genotype (**Fig 8a**).

328 The differentiation dynamics of the four hiPSC-derived SC lines were assessed by RNAseq at
329 two time points. We chose day (d)18, a committed SCP-like stage, and d31, for a stage more
330 analogous to immature SC (**Fig 8a**). Due to their different phenotypes *in vitro*, we analyzed the
331 mutant lines both together and individually for DEGs relative to control lines (**Table S3**).
332 Pathway analyses of 380 DEGs common to both mutant cell lines at D31 using the human
333 Reactome database [72] highlighted their unexpected downregulation of transcripts associated
334 with epidermal cornification, including eight keratin genes (REAC:R-HSA-6809371; **Fig 8c**;
335 **Table S3**). Another significantly downregulated pathway was "EGR2 and SOX10-mediated
336 initiation of SC myelination" (REAC:R-HSA-9619665, **Fig 8c-d**). Among the downregulated
337 transcripts therein were *EGR2* itself, *MBP*, *PRX* and *LAMA2* (encoding the alpha-2 chain of
338 laminin-211, a major component of SC basal lamina).

339 In contrast, the transcription factor *POU3F2* was commonly upregulated in CFC patient-
340 derived cell lines at both stages analyzed; **Table S3**). Functionally redundant *Pou3f1* and
341 *Pou3f2* are transiently required in early murine SC, peaking in the first week after birth [73].
342 Annotations associated with all genes upregulated in concert with *POU3F2* in human SC
343 differentiated from each CFC line, compared to the control hiPSC, evoked the multipotency of
344 neural crest-derived SCPs. Significant associations included the term "melanoma" and the
345 proteome of an amelanotic, *BRAF*^{V600E}-mutated melanoma cell line A2058; cell line proteomes
346 from a *P53*-mutated lung neuroendocrine carcinoma (NCI-H446) and a *NRAS*^{Q61L}-mutated
347 neuroblastoma (SK-N-AS), as well as genes transcribed in "visceral" (parasympathetic)
348 autonomic neurons **(Fig 8e**). These observations suggest that maintenance of MAPK signaling
349 after birth in immature SC of both mice and humans prolongs their co-expression of
350 transcriptional programs typical of other neural crest lineages [74,75]. Both *in vitro* and *in vivo*, the
351 maintenance of otherwise physiologically transient MAPK pathway activation in cycling SC
352 seems to prevent their terminal differentiation.

353

Discussion

A new model of RASopathy endophenotypes

In this work, we have demonstrated that constitutive activation of BRAF-mediated signaling in only a subpopulation of NC-derived cells is sufficient to phenocopy a subset of systemic effects found across multiple germline RASopathy syndromes. One major outcome was rapid onset of hyperplastic neuropathy, evocative of that described as “hypertrophic” in case reports and small patient series [25,27,76–79], but which had not been reported in systemic RASopathy animal models [80]. Clinical signs of neuropathy should therefore be more systematically sought across all RASopathy patients, as they converge mechanistically on sustained ERK1/2 activation in Schwann cells.

Severe feeding difficulties are frequent in *BRAF*-associated RASopathies, irrespective of the specific variant [25,81–83]. However, despite their motility issues, Mpz-*Braf* mice ate normally (see Fig 1f). No megacolon was observed in our mouse model at any age as a sign of gut dysmotility, while somatic growth delay due to Igf1 deficiency was well underway before weaning. Enteric glia may not have been efficiently targeted by the *Mpz*-Cre allele [84], as *Mpz* is transcribed at a basal level in postmigratory, Sox10-expressing SCP [85] but more strongly upregulated in myelinating SC [40,86]. Remarkably, some transcripts co-expressed specifically in adult mouse enteric glia, such as *Plp1* and *Gfap* [87], are upregulated over time in Mpz-*Braf* sciatic nerves (Supplemental Table S3). As enteric glia are also NC progeny, this observation suggests that the observed repair phenotype reverts SCPs to a state of commitment that precedes specialization of peripheral glial subtypes.

Unexpected endocrine phenotypes

The conditional Mpz-*Braf* mouse, with its pre-weaning growth retardation, also complements a series of RASopathy animal models that fail to thrive in the early postnatal period following germline mutations in *Kras* [88], *Braf* [89,90,68,69], *Raf1* [91], *Ptpn11* [92] or *Sos1* [93]. No other models were mosaics that restricted strong MAPK activation to cells having expressed *Mpz*. It was thus a surprise that somatic growth was affected.

Mpz-*Braf* mice do not display an effective second growth spurt, normally initiated by Gh from 12-25 days after birth [94], despite initially normal *Ghrhr* and *Gh* transcription by the pituitary. Our results implicate secondary, liver-produced Igf1 deficiency as responsible for small body size in both sexes, but not for the male cryptorchidism (undescended testicles). Postnatal *Igf1*-null mice, when they survive (5-15% depending on background), grow to less than half the size of wildtype littermates; no cryptorchidism was described despite infertility [95,96]. Knock-in of a conditional *Igf1* allele into the natural, but inoperative, *Igf1* locus in *Igf1*-null mice, followed by

388 activation of liver-restricted transcription, is sufficient to restore both body size and fertility to
389 both sexes [97].

390 Cryptorchidism affects the majority of males with RASopathies [6,98]; it is less frequent among
391 germline *BRAF*- or *RAF1*-mutated patients in one series than for other RASopathy genes [99].
392 This implies that a pathogenic threshold of maximal MAPK activation is less often attained by
393 typical RAF family gene mutations in the germline than by mutations in the upstream effectors
394 *PTPN11*, *RIT1* or *SOS2*. Furthermore, the *Mpz*-Braf model displays a fully penetrant
395 phenotype, despite *Mpz* not being expressed by germ cells in mice or humans. Surgical section
396 of the rat genitofemoral nerve even after puberty leads to neuropathic degeneration of the
397 cremaster muscle, partial testicular ascent and reduced fertility [100]. Our observations therefore
398 provide indirect support to the hypothesis that peripheral nerve myelination is also required to
399 preserve testicular descent and fertility [101,102].

400 Finally, NS patients and the *Ptpn11*$^{D61G/+}$ RASopathy mouse model for NS also show low Igf1
401 levels during post-weaning growth. Uncoupling Gh stimulation from Igf1 release by sustained
402 MAPK signaling downstream of Ghr is reminiscent of the uncoupling of Nrg1 stimulation from
403 Erbb3-mediated SC differentiation to a myelinating phenotype, and suggests that constitutive
404 somatic activation of MAPK-mediated pathways may lead to other human disorders. Evidence
405 for this also comes from the identification of septo-optic dysplasia in some CFC patients with
406 *BRAF* gain-of-function mutations, phenocopied in terms of preventing terminal differentiation
407 of the pituitary gland by conditional expression of murine *Braf* V600E/+ or *Braf* Q241R/+ in
408 Prop1-expressing pituitary progenitors [2].

409 A form of murine congenital hypomyelinating neuropathy

410 Dejerine-Sottas syndrome, or CMT3, is a demyelinating congenital peripheral neuropathy
411 caused by mutations in *MPZ*, *EGR2*, *PMP22* or *PRX* [103]. CMT3 often presents distal sensory
412 loss, profuse SC proliferation and as per its first report in 1893, enlarged, “gelatinous”
413 peripheral nerves that are more affected in the legs than the arms [104]. The tremor and
414 locomotor troubles we observed in Mpz-*Braf* mice also first affected the hindlimbs without
415 extending to other body areas before 6 weeks of age. Nonetheless, sensory and motor nerves
416 around the body were visibly enlarged on autopsy. These observations in the absence of
417 apparent suffering (aversion, unkempt fur, flattened ears, etc.) make the weanling Mpz-*Braf*
418 mouse a tractable model in which to carry out further behavioral or electrophysiological studies
419 of early RASopathy-associated neuropathy, or to test interventional therapies [105]. Our findings
420 support the Schwann cell as the initiator of these neuromuscular outcomes.

421 Oligopotent Schwann cell (SC) precursors, persisting both in ganglia and along postnatal
422 nerves, were first identified when they transdifferentiated into nerve-derived melanocytes after

423 nerve injury [74]. Mosaic expression of an oncogenic *BRAF* p.V600E variant causes a somatic
424 RASopathy in humans, congenital melanocytic nevus syndrome, that is not associated with
425 peripheral neuropathy [106,107]. Instead, bipotent progenitors proliferate *in utero* before settling
426 on a superficially differentiated skin phenotype after birth. In contrast, when induced
427 conditionally in either murine melanocyte progenitors with a tyrosinase-driven *Cre*, $Braf^{V600E}$
428 causes mid-gestational death with complete penetrance due to heart malformations [19].
429 Tyrosinase is expressed in mid-gestational NC cells before restriction to human postnatal
430 bipotent Schwann-melanocytes [108], and only expressed by a small minority of postnatal cardiac
431 melanocytes in mice [109]. It will be interesting to investigate if tyrosinase is inappropriately
432 maintained in cardiac NC cells after constitutive MAPK activation. Furthermore, *BRAF*
433 p.V600E oncogenic variants are also found in somatic, segmental lymphatic and vascular
434 malformations [110,111]. One of the earliest (but recent) case reports of arteriovenous
435 malformation with this genotype was in conjunction with a large intracranial gliosarcoma,
436 derived from brain progenitors capable of giving rise to myelinating and non-myelinating glia
437 [112]. Sustained MAPK signaling in multipotent cells therefore prevents terminal differentiation in
438 multiple prenatal and postnatal situations. This induces functional deficiencies despite ongoing
439 progenitor proliferation.

440 In our assay of human Schwann cell differentiation, the CFC patient cell line least capable of
441 acquiring a SC phenotype, 138C, instead maintained strong expression at day 31 of *HOX*
442 family genes of the first six paralogue groups as well as *PHOX2B*, a master transcription factor
443 for autonomic neurons and SCPs. Cells from both patients showed common significant
444 upregulation of *HOXB2*, *ARG2* and *SALL1* (**Table S3**). *ARG2* encodes arginase-2, a metabolic
445 enzyme significantly upregulated in response to tumor macrophage-stimulated ERK1/2 activity
446 in neuroblastoma [113]. This neural crest-derived congenital cancer derives from multipotent
447 Schwann/autonomic progenitors and usually presents in early childhood [114,115]. In high-risk
448 forms, tumor cells maintain an undifferentiated mesenchymal phenotype associated with *JUN*,
449 at the expense of *PHOX2B* expression [116]. *SALL1* (Spalt-like transcription factor 1) is a widely
450 transcribed but determinant transcription factor of central nervous system macrophages known
451 as microglia, but is not present in bone marrow-derived peripheral microglia [117]. Altogether, we
452 have shown that patient-derived, $BRAF^{Q257R}$-expressing NC cells are at a stochastic
453 disadvantage in assuming a differentiated SC phenotype *in vitro*, as compared to *BRAF*-
454 wildtype cells. Patient-derived nerve biopsies taken for molecular diagnosis would be
455 necessary to confirm these findings with a prospective study in unresolved cases of either
456 RASopathies or early-onset CMT.

457 # Methods

458 ## Ethical statement

459 This study complies with all relevant ethical regulations. Animal care and experiments were in
460 accordance with French and European legislation and approved by the French ACUC (C2EA-
461 14; project numbers 37-08102012 and 9522-2017040517496865v5). Human iPSC studies
462 adhered to the Declaration of Helsinki [118] and French bioethics law (2021-1017)[119] consistent
463 with our institutional review board protocols.

464 ## Mouse breeding and genotyping

465 Transgenic *P0-Cre*$^{+/°}$; *Braf*$^{V600E/+}$ and *Krox20-Cre*$^{+/°}$; *Braf*$^{V600E/+}$ mice were generated by
466 crossing *LSL-Braf*$^{V600E/+}$ mice [15] (RRID:IMSR_JAX:017928) with P0(Mpz)-*Cre*
467 (RRID:IMSR_JAX:017927) [39,120] or Krox20-*Cre* (RRID:IMSR_JAX:025744) [121] drivers.
468 Genotyping was performed by PCR (see Supplementary Methods). Mice were housed under
469 standard conditions (12-hour light/dark cycles, *ad libitum* access to food/water).

470 ## Western Blots

471 Sciatic nerve lysates were prepared in RIPA buffer with protease inhibitors, separated by 12%
472 SDS-PAGE, and probed with antibodies against phospho-Erk1/2 (RRID:AB_331646), Erk1/2
473 (RRID:AB_330744), c-Jun (RRID:AB_2130165) and Gapdh (RRID:AB_2107445). Alternately,
474 primary antibodies to Shh (RRID:AB_528466)[122], Erbb3 (RRID:AB_358277), Egr2
475 (RRID:AB_10862073), alpha-tubulin (RRID:AB_2241126), vimentin (RRID:AB_2881439) or
476 vinculin (RRID:AB_10603627) were used. Signals were detected using relevant secondary
477 antibodies (RRID:AB_330924 and RRID:AB_2099233) followed by chemiluminescence
478 detection and quantified with ImageJ v.1.54f.

479 ## Culture and differentiation of human pluripotent stem cells (hiPSC)

480 Two female patients with cardio-facio-cutaneous (CFC) syndrome bearing a heterozygous
481 germline *BRAF* Q257R variant, or their legal guardians, provided written consent as approved
482 by the UCSF Human Research Protection Program (CHR #10-02794), to produce the human
483 induced pluripotent stem cell (hiPSC) lines, RMK0056C and RMK0138C, as described [70]. The
484 AG08H and HFF15 clones of healthy donor male hiPSC were derived from commercial cell
485 lines consented for research, AG08498 (RRID:CVCL_1Y51) and HFF-1 SCRC-1041
486 (RRID:CVCL_3285) as described [123]. Clones were initially grown in mTeSR1 (Stemcell) on
487 human ES cell-qualified Matrigel™ before cryopreservation. Thawed hiPSC were cultured on
488 Synthemax II-SC (Corning) at 0.025 mg/mL and maintained with daily changes of StemMACS
489 iPS-Brew XF (Miltenyi Biotec). At 60-80% confluence, they were passed with ReleSR
490 (StemCell Technologies), with 10 µM Y-27632 for the first day. Differentiation of hiPSCs into

491 SC [71] was initiated at 60% confluence and passed every 6 days until day 31. Thereafter, upon
492 90% confluence, they were split 1:2.

493 RNA sequencing and analyses

494 Sciatic nerves and pituitary glands from WT or *Braf*$^{V600E/+}$ animals, and pellets of WT or
495 *BRAF*$^{Q257R/+}$ hiPSC-derived SCP and immature Schwann cells (iSC) were stored at -80°C.
496 Tissues were lysed in the FastPrep-24 homogenizer (MP Biomedicals) and total RNA
497 extracted with the RNeasy Lipid Tissue Mini (Qiagen) or, for cell pellets, NucleoSpin RNA Plus
498 S (Macherey-Nagel) kits. RNA concentrations were measured on a NanoDrop TM 1000
499 Spectrophotometer (ThermoFisher). Libraries were prepared with the KAPA mRNA HyperPrep
500 kit (Roche) and sequenced on a NovaSeq 6000 (Illumina). Quality was assessed using fastQC
501 (v0.11.5). Raw sequencing reads were aligned to GRCm39/GRCh38 using STAR (v2.7.2b).
502 Bam files were indexed and sorted with Samtools (v1.7). After mapping, reads per feature
503 (Ensembl or GENCODE v34 annotations for mouse or human data, respectively) were
504 determined using StringTie v2.1.6, and differential expression analyzed with a Wald test in
505 DESeq2 (v1.34.0; FDR < 0.05). Data visualization made use of R packages Pheatmap and
506 EnhancedVolcano [124]. Expression-dependent enrichment analyses were conducted with Gene
507 Set Enrichment Analysis (GSEA) v4.3.2 [125] using mouse Wikipathway and human Reactome
508 databases, otherwise with g:Profiler [126] or Enrichr-KG [127], interrogating quantitative proteomics
509 of the Cancer Cell Line Encyclopedia [128] KEGG, Reactome, Gene Ontology datasets.

510 These were significantly enriched by Enrichr-KG [127], using databases of annotations related to
511 human disease [129], and a large single-cell atlas of developmental human gene expression [130].

512

513

514 Nerve and fiber immunostaining

515 Sciatic nerves were fixed in 4% buffered paraformaldehyde and stained with primary
516 antibodies to Mbp (RRID:AB_94975); Ki-67 (RRID:AB_10854564); Caspr (RRID:AB_869934);
517 Sox10 (RRID:AB_2941085); Pmp2 (RRID:AB_2166978); Erbb3 (RRID:AB_358277); S100b
518 (RRID:AB_1856538); or Shh (RRID:AB_528466)[122], followed by secondary antibodies and
519 DAPI counterstaining. Further details are in the Supplemental Methods. Image stacks of
520 teased fibers were acquired with a spinning disk confocal microscope (Nikon SoRa) and NIS-
521 Elements software and nerve images on a Zeiss LSM800 with Airyscan and Zen software v2.3.

522 ### Transmission electron microscopy (TEM) and morphometry

523 Sciatic nerves were fixed in 2% PFA + 2.5% glutaraldehyde, post-fixed with 1% OsO_4,
524 contrasted in 1% uranyl acetate before Epon resin embedding. Semi-thin sections at 1 µm
525 were counterstained with toluidine blue. Ultra-thin sections were imaged on an FEI Morgagni
526 120 kv microscope. Myelin morphological parameters were analyzed with MyelTracer [43]. Axon
527 density was assessed with ImageJ using the semi-thin sections.

528 Statistics

529 Statistical analyses were performed with Prism v10.2.0 (GraphPad), using unpaired Mann-
530 Whitney or two-way ANOVA non-parametric tests. For multiple comparisons, two-way ANOVA
531 followed by Šidák's post-hoc tests, or Student t-tests followed by Benjamini-Hochberg
532 adjustment, were used. Mendelian segregation was assessed with a chi-square contingency
533 test. Data are presented as mean ± SEM; significance: * $p < 0.05$; ** $p < 0.01$; *** $p < 0.001$;
534 **** $p < 0.0001$.

535 Data availability

536 Raw and processed RNA-sequencing data from this study have been deposited to the Gene
537 Expression Omnibus (GEO) and assigned the accession identifiers GSE262047 and
538 GSE262048.

539 Websites

540 "Catalogue Of Somatic Mutations In Cancer" (COSMIC), https://cancer.sanger.ac.uk/cosmic [1].

541 Rare disease ORPHA codes are maintained at https://www.orpha.net and available on
542 https://www.orphadata.com/ [18].

543 fastQC (v0.11.5) is available at https://www.bioinformatics.babraham.ac.uk/projects/fastqc/
544 and EnhancedVolcano at https://bioconductor.org/packages/EnhancedVolcano.

545 NIH Fiji/ImageJ software (https://imagej.net/ij/) is available from https://imagej.net/ij/.

546 Author contributions

547 E.M. wrote the first draft, performed and analyzed experiments; D.A. provided analyses,
548 performed experiments and extensively revised the manuscript; P.Q., G.M. and M.M.
549 performed experiments; N.B.M. and V.D. provided protocols and guidance; C.E.Y. and N.B.
550 provided control hiPSC lines and guidance; L.A.W. provided patient hiPSC lines; A.B. provided
551 constructive criticism and funding; H.C.E. supervised the experiments, provided funding, wrote
552 and revised the article.

553 # Competing interests

554 The authors declare no competing interests.

555 # Acknowledgements

556 We are grateful to C. Humbert, C. Castro, N. Trévisiol and C. Aubert of the MMG Genomics
557 and Bioinformatics facility (GBiM) for assistance with RNAseq and analyses; Dr. F. Magdinier
558 and O. Hadadeh of the Marseille Stem Cell (MaSC) core facility for control hiPSC cell lines and
559 their quality control; Dr. T.-T. Mac, Adeline Querdray and Dr. T. Fauquier for their technical
560 assistance and advice; the PiCSL-France BioImaging core facility, supported by ANR-10-
561 INBS-04, and Dr. C. Leterrier and Dr. L. Fourel of the Institute of NeuroPhysiopathology,
562 CNRS-Aix Marseille University, for their assistance with spinning-disk confocal microscopy.

563 # Funding

564 The authors declare that they have no conflicts of interest. This work was made possible by
565 the Association Française contre les Myopathies (AFM-Téléthon) grant 'MoThARD' to VD and
566 HCE, the National Institutes of Health New Innovator award (1DP2OD007449) to LAW, and
567 Horizon Europe HORIZON-MISS-2021-CANCER-02-03 MELCAYA (101096667) to HCE. EM
568 was supported by the AFM-Téléthon, the Asociación Española de Nevus Gigante Congénito
569 (AsoNevus, Spain), Naevus 2000 France-Europe (France) and the Marseille Rare Diseases
570 Institute (MarMaRa) of Aix-Marseille University.

571 # References

572 1. Sondka, Z. *et al.* COSMIC: a curated database of somatic variants and clinical data for
573 cancer. *Nucleic Acids Res.* **52**, D1210–D1217 (2024).
574 2. Gualtieri, A. *et al.* Activating mutations in BRAF disrupt the hypothalamo-pituitary axis
575 leading to hypopituitarism in mice and humans. *Nat. Commun.* **12**, 2028 (2021).
576 3. Hilal, N., Chen, Z., Chen, M. H. & Choudhury, S. RASopathies and cardiac
577 manifestations. *Front. Cardiovasc. Med.* **10**, 1176828 (2023).
578 4. Jaeger, Z. J. *et al.* RASopathies. Part II: Cutaneous and extracutaneous manifestations.
579 *J. Am. Acad. Dermatol.* S0190-9622(25)02340–0 (2025) doi:10.1016/j.jaad.2025.01.106.
580 5. Kang, M. & Lee, Y.-S. The impact of RASopathy-associated mutations on CNS
581 development in mice and humans. *Mol. Brain* **12**, 96 (2019).

582 6. Rauen, K. A. The RASopathies. *Annu. Rev. Genomics Hum. Genet.* **14**, 355–369 (2013).
583 7. Siano, M. A. *et al.* Endocrine system involvement in patients with RASopathies: A case
584 series. *Front. Endocrinol.* **13**, (2022).
585 8. Tartaglia, M., Aoki, Y. & Gelb, B. D. The molecular genetics of RASopathies: An update
586 on novel disease genes and new disorders. *Am. J. Med. Genet. C Semin. Med. Genet.*
587 **190**, 425–439 (2022).
588 9. Carli, D., Resta, N., Ferrero, G. B., Ruggieri, M. & Mussa, A. Mosaic RASopathies: A
589 review of disorders caused by somatic pathogenic variants in the genes of the
590 RAS/MAPK pathway. *Am. J. Med. Genet. C Semin. Med. Genet.* **190**, 520–529 (2022).
591 10. Kratz, C. P., Rapisuwon, S., Reed, H., Hasle, H. & Rosenberg, P. S. Cancer in Noonan,
592 Costello, Cardiofaciocutaneous and LEOPARD Syndromes. *Am. J. Med. Genet. Part C*
593 **157**, 83–89 (2011).
594 11. Peltonen, S. *et al.* Pediatric malignancies in neurofibromatosis type 1: A population-based
595 cohort study. *Int. J. Cancer* **145**, 2926–2932 (2019).
596 12. Davies, H. *et al.* Mutations of the BRAF gene in human cancer. *Nature* **417**, 949–954
597 (2002).
598 13. Kawakami, H. *et al.* Mutant BRAF Upregulates MCL-1 to Confer Apoptosis Resistance
599 that Is Reversed by MCL-1 Antagonism and Cobimetinib in Colorectal Cancer. *Mol.*
600 *Cancer Ther.* **15**, 3015–3027 (2016).
601 14. Xing, M. BRAF mutation in thyroid cancer. *Endocr. Relat. Cancer* **12**, 245–262 (2005).
602 15. Mercer, K. *et al.* Expression of endogenous oncogenic V600EB-raf induces proliferation
603 and developmental defects in mice and transformation of primary fibroblasts. *Cancer Res.*
604 **65**, 11493–11500 (2005).
605 16. Haling, J. R. *et al.* Structure of the BRAF-MEK Complex Reveals a Kinase Activity
606 Independent Role for BRAF in MAPK Signaling. *Cancer Cell* **26**, 402–413 (2014).
607 17. Yao, Z. *et al.* BRAF Mutants Evade ERK-Dependent Feedback by Different Mechanisms
608 that Determine Their Sensitivity to Pharmacologic Inhibition. *Cancer Cell* **28**, 370–383
609 (2015).

610 18. Aymé, S., Bellet, B. & Rath, A. Rare diseases in ICD11: making rare diseases visible in
611 health information systems through appropriate coding. *Orphanet J. Rare Dis.* **10**, 35
612 (2015).
613 19. Dhomen, N. *et al.* Inducible expression of (V600E) Braf using tyrosinase-driven Cre
614 recombinase results in embryonic lethality. *Pigment Cell Melanoma Res.* **23**, 112–20
615 (2010).
616 20. Gripp, K. W. *et al.* Further delineation of the phenotype resulting from BRAF or MEK1
617 germline mutations helps differentiate cardio-facio-cutaneous syndrome from Costello
618 syndrome. *Am. J. Med. Genet. A.* **143A**, 1472–1480 (2007).
619 21. Koudova, M., Seemanova, E. & Zenker, M. Novel BRAF mutation in a patient with
620 LEOPARD syndrome and normal intelligence. *Eur. J. Med. Genet.* **52**, 337–340 (2009).
621 22. Nava, C. *et al.* Cardio-facio-cutaneous and Noonan syndromes due to mutations in the
622 RAS/MAPK signalling pathway: genotype-phenotype relationships and overlap with
623 Costello syndrome. *J. Med. Genet.* **44**, 763–71 (2007).
624 23. Nyström, A.-M. *et al.* Noonan and cardio-facio-cutaneous syndromes: two clinically and
625 genetically overlapping disorders. *J. Med. Genet.* **45**, 500–506 (2008).
626 24. Tartaglia, M., Gelb, B. D. & Zenker, M. Noonan syndrome and clinically related disorders.
627 *Best Pract. Res. Clin. Endocrinol. Metab.* **25**, 161–179 (2011).
628 25. Manci, E. A. *et al.* Cardiofaciocutaneous syndrome (CFC) with congenital peripheral
629 neuropathy and nonorganic malnutrition: an autopsy study. *Am. J. Med. Genet. A.* **137**,
630 1–8 (2005).
631 26. De Ridder, W., van Engelen, B. & van Alfen, N. Neurological features of Noonan
632 syndrome and related RASopathies: Pain and nerve enlargement characterized by nerve
633 ultrasound. *Am. J. Med. Genet. A.* **188**, 1801–1807 (2022).
634 27. Draaisma, F. *et al.* Hypertrophic neuropathy: a possible cause of pain in children with
635 Noonan syndrome and related disorders. *Eur. J. Pediatr.* **182**, 3789–3793 (2023).

636 28. Callegari, I. *et al.* Mutation update for myelin protein zero-related neuropathies and the
637 increasing role of variants causing a late-onset phenotype. *J. Neurol.* **266**, 2629–2645
638 (2019).
639 29. Ishii, A., Furusho, M. & Bansal, R. Sustained activation of ERK1/2 MAPK in
640 oligodendrocytes and schwann cells enhances myelin growth and stimulates
641 oligodendrocyte progenitor expansion. *J. Neurosci. Off. J. Soc. Neurosci.* **33**, 175–186
642 (2013).
643 30. Sheean, M. E. *et al.* Activation of MAPK overrides the termination of myelin growth and
644 replaces Nrg1/ErbB3 signals during Schwann cell development and myelination. *Genes*
645 *Dev.* **28**, 290–303 (2014).
646 31. Belin, S. *et al.* Neuregulin 1 type III improves peripheral nerve myelination in a mouse
647 model of congenital hypomyelinating neuropathy. *Hum. Mol. Genet.* **28**, 1260–1273
648 (2019).
649 32. Ishii, A., Furusho, M., Dupree, J. L. & Bansal, R. Strength of ERK1/2 MAPK Activation
650 Determines Its Effect on Myelin and Axonal Integrity in the Adult CNS. *J. Neurosci. Off.*
651 *J. Soc. Neurosci.* **36**, 6471–6487 (2016).
652 33. Pipis, M., Rossor, A. M., Laura, M. & Reilly, M. M. Next-generation sequencing in
653 Charcot–Marie–Tooth disease: opportunities and challenges. *Nat. Rev. Neurol.* **15**, 644–
654 656 (2019).
655 34. Eid, S. A. *et al.* Single-cell RNA-seq uncovers novel metabolic functions of Schwann cells
656 beyond myelination. *J. Neurochem.* **166**, 367–388 (2023).
657 35. Geren, B. B. The formation from the schwann cell surfaceof myelin in the peripheral
658 nerves of chick embryos. *Exp. Cell Res.* **7**, 558–562 (1954).
659 36. Le Douarin, N., Dulac, C., Dupin, E. & Cameron-Curry, P. Glial cell lineages in the neural
660 crest. *Glia* **4**, 175–84 (1991).
661 37. Etchevers, H. C., Dupin, E. & Le Douarin, N. M. The diverse neural crest: from
662 embryology to human pathology. *Development* **146**, (2019).

663 38. Kelnar, C. J. H. Noonan syndrome: the hypothalamo-adrenal and hypothalamo-gonadal
664 axes. *Horm. Res.* **72 Suppl 2**, 24–30 (2009).
665 39. Feltri, M. L. *et al.* A novel P 0 glycoprotein transgene activates expression of lac Z in
666 myelin-forming Schwann cells. *Eur. J. Neurosci.* **11**, 1577–1586 (1999).
667 40. Hagedorn, L., Suter, U. & Sommer, L. P0 and PMP22 mark a multipotent neural crest-
668 derived cell type that displays community effects in response to TGF-beta family factors.
669 *Development* **126**, 3781–3794 (1999).
670 41. Lundberg, E., Kriström, B., Jonsson, B., Albertsson-Wikland, K., & study group. Growth
671 hormone (GH) dose-dependent IGF-I response relates to pubertal height gain. *BMC*
672 *Endocr. Disord.* **15**, 84 (2015).
673 42. Alvey, L. M., Jones, J. F. X., Tobin-O'Brien, C. & Pickering, M. Bands of Fontana are
674 caused exclusively by the sinusoidal path of axons in peripheral nerves and predict axon
675 path; evidence from rodent nerves and physical models. *J. Anat.* **234**, 165–178 (2019).
676 43. Kaiser, T. *et al.* MyelTracer: A Semi-Automated Software for Myelin g-Ratio
677 Quantification. *eNeuro* **8**, ENEURO.0558-20.2021 (2021).
678 44. Kozlowski, M. M. *et al.* Pmp2+ Schwann Cells Maintain the Survival of Large-Caliber
679 Motor Axons. *J. Neurosci.* **45**, e1362242025 (2025).
680 45. Woodhoo, A. & Sommer, L. Development of the Schwann cell lineage: from the neural
681 crest to the myelinated nerve. *Glia* **56**, 1481–1490 (2008).
682 46. Kuhlbrodt, K., Herbarth, B., Sock, E., Hermans-Borgmeyer, I. & Wegner, M. Sox10, a
683 novel transcriptional modulator in glial cells. *J. Neurosci.* **18**, 237–250 (1998).
684 47. Gerdes, J. *et al.* Cell cycle analysis of a cell proliferation-associated human nuclear
685 antigen defined by the monoclonal antibody Ki-67. *J. Immunol. Baltim. Md 1950* **133**,
686 1710–1715 (1984).
687 48. Miller, I. *et al.* Ki67 is a Graded Rather than a Binary Marker of Proliferation versus
688 Quiescence. *Cell Rep.* **24**, 1105-1112.e5 (2018).
689 49. Poitelon, Y., Kopec, A. M. & Belin, S. Myelin Fat Facts: An Overview of Lipids and Fatty
690 Acid Metabolism. *Cells* **9**, 812 (2020).

691 50. Ohashi, K. *et al.* Early embryonic lethality caused by targeted disruption of the 3-hydroxy-
692 3-methylglutaryl-CoA reductase gene. *J. Biol. Chem.* **278**, 42936–42941 (2003).
693 51. Maldonado, E. N., Alderson, N. L., Monje, P. V., Wood, P. M. & Hama, H. FA2H is
694 responsible for the formation of 2-hydroxy galactolipids in peripheral nervous system
695 myelin. *J. Lipid Res.* **49**, 153–161 (2008).
696 52. Topilko, P. *et al.* Krox-20 controls myelination in the peripheral nervous system. *Nature*
697 **371**, 796–799 (1994).
698 53. Peirano, R. I., Goerich, D. E., Riethmacher, D. & Wegner, M. Protein zero gene
699 expression is regulated by the glial transcription factor Sox10. *Mol. Cell. Biol.* **20**, 3198–
700 3209 (2000).
701 54. Jessen, K. R. & Mirsky, R. Negative regulation of myelination: relevance for development,
702 injury, and demyelinating disease. *Glia* **56**, 1552–1565 (2008).
703 55. Hong, J. *et al.* PMP2 regulates myelin thickening and ATP production during
704 remyelination. *Glia* **72**, 885–898 (2024).
705 56. Stassart, R. M. *et al.* A role for Schwann cell-derived neuregulin-1 in remyelination. *Nat.*
706 *Neurosci.* **16**, 48–54 (2013).
707 57. Heming, M. *et al.* Multi-omic identification of perineurial hyperplasia and lipid-associated
708 nerve macrophages in human polyneuropathies. *Nat. Commun.* **16**, 7872 (2025).
709 58. Serra-Nédélec, A. D. R. *et al.* Noonan syndrome-causing SHP2 mutants inhibit insulin-
710 like growth factor 1 release via growth hormone-induced ERK hyperactivation, which
711 contributes to short stature. *Proc. Natl. Acad. Sci.* **109**, 4257–4262 (2012).
712 59. Arthur-Farraj, P. J. *et al.* Changes in the Coding and Non-coding Transcriptome and DNA
713 Methylome that Define the Schwann Cell Repair Phenotype after Nerve Injury. *Cell Rep.*
714 **20**, 2719–2734 (2017).
715 60. Parkinson, D. B. *et al.* c-Jun is a negative regulator of myelination. *J. Cell Biol.* **181**, 625–
716 637 (2008).

717 61. Piirsoo, M., Kaljas, A., Tamm, K. & Timmusk, T. Expression of NGF and GDNF family
718 members and their receptors during peripheral nerve development and differentiation of
719 Schwann cells in vitro. *Neurosci. Lett.* **469**, 135–140 (2010).
720 62. da Costa, M. C., Trentin, A. G. & Calloni, G. W. FGF8 and Shh promote the survival and
721 maintenance of multipotent neural crest progenitors. *Mech. Dev.* **154**, 251–258 (2018).
722 63. Hashimoto, M. *et al.* Neuroprotective effect of sonic hedgehog up-regulated in Schwann
723 cells following sciatic nerve injury. *J. Neurochem.* **107**, 918–927 (2008).
724 64. Takahashi, K. *et al.* Immunohistochemical study on the distribution of alpha and beta
725 subunits of S-100 protein in human neoplasm and normal tissues. *Virchows Arch. B Cell*
726 *Pathol. Incl. Mol. Pathol.* **45**, 385–396 (1984).
727 65. Huang, L. *et al.* c-Jun gene-modified Schwann cells: upregulating multiple neurotrophic
728 factors and promoting neurite outgrowth. *Tissue Eng. Part A* **21**, 1409–1421 (2015).
729 66. Carroll, S. L., Miller, M. L., Frohnert, P. W., Kim, S. S. & Corbett, J. A. Expression of
730 neuregulins and their putative receptors, ErbB2 and ErbB3, is induced during Wallerian
731 degeneration. *J. Neurosci. Off. J. Soc. Neurosci.* **17**, 1642–1659 (1997).
732 67. Perlson, E. *et al.* Vimentin-dependent spatial translocation of an activated MAP kinase in
733 injured nerve. *Neuron* **45**, 715–726 (2005).
734 68. Inoue, S.-I. *et al.* New BRAF knockin mice provide a pathogenetic mechanism of
735 developmental defects and a therapeutic approach in cardio-facio-cutaneous syndrome.
736 *Hum. Mol. Genet.* **23**, 6553–6566 (2014).
737 69. Moriya, M. *et al.* Adult mice expressing a Braf Q241R mutation on an ICR/CD-1
738 background exhibit a cardio-facio-cutaneous syndrome phenotype. *Hum. Mol. Genet.* **24**,
739 7349–7360 (2015).
740 70. Yeh, E. *et al.* Patient-derived iPSCs show premature neural differentiation and neuron
741 type-specific phenotypes relevant to neurodevelopment. *Mol. Psychiatry* **23**, 1687–1698
742 (2018).
743 71. Hörner, S. J. *et al.* hiPSC-Derived Schwann Cells Influence Myogenic Differentiation in
744 Neuromuscular Cocultures. *Cells* **10**, 3292 (2021).

745 72. Milacic, M. *et al.* The Reactome Pathway Knowledgebase 2024. *Nucleic Acids Res.* **52**,
746 D672–D678 (2024).
747 73. Jaegle, M. *et al.* The POU proteins Brn-2 and Oct-6 share important functions in Schwann
748 cell development. *Genes Dev.* **17**, 1380–1391 (2003).
749 74. Adameyko, I. *et al.* Schwann cell precursors from nerve innervation are a cellular origin
750 of melanocytes in skin. *Cell* **139**, 366–379 (2009).
751 75. Furlan, A. *et al.* Multipotent peripheral glial cells generate neuroendocrine cells of the
752 adrenal medulla. *Science* **357**, eaal3753 (2017).
753 76. Ando, Y. *et al.* A novel KRAS gene mutation of Noonan syndrome with severe peripheral
754 nerve hypertrophy. *J. Neurol. Sci.* **333**, e605 (2013).
755 77. DeRoos, S. T., Ryan, M. M. & Ouvrier, R. A. Peripheral neuropathy in
756 cardiofaciocutaneous syndrome. *Pediatr. Neurol.* **36**, 250–252 (2007).
757 78. Maridet, C., Sole, G., Morice-Picard, F. & Taieb, A. Hypertrophic neuropathy in Noonan
758 syndrome with multiple lentigines. *Am. J. Med. Genet. A.* **170**, 1570–1572 (2016).
759 79. Vizcaino, M. A. *et al.* Localized Hypertrophic Neuropathy as a Neoplastic Manifestation
760 of KRAS-Mediated RASopathy. *J. Neuropathol. Exp. Neurol.* **79**, 647–651 (2020).
761 80. Hernández-Porras, I. & Guerra, C. Modeling RASopathies with Genetically Modified
762 Mouse Models. *Methods Mol. Biol. Clifton NJ* **1487**, 379–408 (2017).
763 81. Allanson, J. E. *et al.* Cardio-facio-cutaneous syndrome: Does genotype predict
764 phenotype? *Am. J. Med. Genet. C Semin. Med. Genet.* **157**, 129–135 (2011).
765 82. Feng, B. *et al.* Molecular and phenotypic spectrum of cardio-facio-cutaneous syndrome
766 in Chinese patients. *Orphanet J. Rare Dis.* **18**, 284 (2023).
767 83. Lee, Y. *et al.* Clinical and molecular spectra of BRAF-associated RASopathy. *J. Hum.*
768 *Genet.* **66**, 389–399 (2021).
769 84. Woods, C. *et al.* Neurons populating the rectal extrinsic nerves in humans express
770 neuronal and Schwann cell markers. *Neurogastroenterol. Motil.* **33**, e14074 (2021).
771 85. Kunke, M. *et al.* SOX10-Mediated Regulation of Enteric Glial Phenotype in vitro and its
772 Relevance for Neuroinflammatory Disorders. *J. Mol. Neurosci.* **75**, 26 (2025).

773 86. Lee, M. J. *et al.* P0 is constitutively expressed in the rat neural crest and embryonic nerves
774 and is negatively and positively regulated by axons to generate non- myelin-forming and
775 myelin-forming Schwann cells, respectively. *Mol. Cell. Neurosci.* **8**, 336–350 (1997).
776 87. Rao, M. *et al.* Enteric glia express proteolipid protein 1 and are a transcriptionally unique
777 population of glia in the mammalian nervous system. *Glia* **63**, 2040–2057 (2015).
778 88. Hernández-Porras, I. *et al.* K-RasV14I recapitulates Noonan syndrome in mice. *Proc.*
779 *Natl. Acad. Sci. U. S. A.* **111**, 16395–16400 (2014).
780 89. Urosevic, J. *et al.* Constitutive activation of B-Raf in the mouse germ line provides a model
781 for human cardio-facio-cutaneous syndrome. *Proc. Natl. Acad. Sci. U. S. A.* **108**, 5015–
782 5020 (2011).
783 90. Andreadi, C. *et al.* The intermediate-activity L597VBRAF mutant acts as an epistatic
784 modifier of oncogenic RAS by enhancing signaling through the RAF/MEK/ERK pathway.
785 *Genes Dev.* **26**, 1945–1958 (2012).
786 91. Wu, X. *et al.* MEK-ERK pathway modulation ameliorates disease phenotypes in a mouse
787 model of Noonan syndrome associated with the Raf1(L613V) mutation. *J. Clin. Invest.*
788 **121**, 1009–1025 (2011).
789 92. Araki, T. *et al.* Mouse model of Noonan syndrome reveals cell type- and gene dosage-
790 dependent effects of Ptpn11 mutation. *Nat. Med.* **10**, 849–857 (2004).
791 93. Chen, P.-C. *et al.* Activation of multiple signaling pathways causes developmental defects
792 in mice with a Noonan syndrome–associated Sos1 mutation. *J. Clin. Invest.* **120**, 4353–
793 4365 (2010).
794 94. Lupu, F., Terwilliger, J. D., Lee, K., Segre, G. V. & Efstratiadis, A. Roles of Growth
795 Hormone and Insulin-like Growth Factor 1 in Mouse Postnatal Growth. *Dev. Biol.* **229**,
796 141–162 (2001).
797 95. Baker, J., Liu, J.-P., Robertson, E. J. & Efstratiadis, A. Role of insulin-like growth factors
798 in embryonic and postnatal growth. *Cell* **75**, 73–82 (1993).
799 96. Powell-Braxton, L. *et al.* IGF-I is required for normal embryonic growth in mice. *Genes*
800 *Dev.* **7**, 2609–2617 (1993).

801 97. Stratikopoulos, E., Szabolcs, M., Dragatsis, I., Klinakis, A. & Efstratiadis, A. The hormonal
802 action of IGF1 in postnatal mouse growth. *Proc. Natl. Acad. Sci.* **105**, 19378–19383
803 (2008).
804 98. Champion, K. J. *et al.* Germline mutation in BRAF codon 600 is compatible with human
805 development: De novo p.V600G mutation identified in a patient with CFC syndrome. *Clin.*
806 *Genet.* **79**, 468–474 (2011).
807 99. Reynolds, G. *et al.* Update on the Clinical and Molecular Characterization of Noonan
808 Syndrome and Other RASopathies: A Retrospective Study and Systematic Review. *Int.*
809 *J. Mol. Sci.* **26**, 3515 (2025).
810 100. Gutiérrez-Pérez, O., Rojas-Castañeda, J. C., Chavez-Saldaña, M., Reyes, G. &
811 Vigueras-Villaseñor, R. M. Infertility in rats subjected to genitofemoral nerve section is not
812 associated with testicular damage. *Andrologia* **46**, 151–157 (2014).
813 101. Prince, F. P. Ultrastructural evidence of indirect and direct autonomic innervation of
814 human Leydig cells: comparison of neonatal, childhood and pubertal ages. *Cell Tissue*
815 *Res.* **269**, 383–390 (1992).
816 102. Tanyel, F. C. Commentary: The fate of germ cells in cryptorchid testis. *Front. Endocrinol.*
817 **15**, 1393040 (2024).
818 103. Pearce, J. M. S. Dejerine-Sottas Disease (Progressive Hypertrophic Polyneuropathy).
819 *Eur. Neurol.* **55**, 115–117 (2006).
820 104. Déjerine, J. & Sottas, J. Sur la névrite interstitielle hypertrophique et progressive de
821 l'enfance. *Comp Rend Soc Biol Paris* **45**, 63–96 (1893).
822 105. Duman, M., Jaggi, S., Enz, L. S., Jacob, C. & Schaeren-Wiemers, N. Theophylline
823 Induces Remyelination and Functional Recovery in a Mouse Model of Peripheral
824 Neuropathy. *Biomedicines* **10**, 1418 (2022).
825 106. Etchevers, H. C. *et al.* Giant congenital melanocytic nevus with vascular malformation
826 and epidermal cysts associated with a somatic activating mutation in BRAF. *Pigment Cell*
827 *Melanoma Res.* **31**, 437–441 (2018).

828 107. Salgado, C. M. *et al.* BRAF Mutations are Also Associated with Neurocutaneous
829 Melanocytosis and Large/Giant Congenital Melanocytic Nevi. *Pediatr. Dev. Pathol.* **18**,
830 1–9 (2015).
831 108. Dusart, P. *et al.* A tissue centric atlas of cell type transcriptome enrichment signatures.
832 2023.01.10.520698 Preprint at https://doi.org/10.1101/2023.01.10.520698 (2023).
833 109. Yajima, I. *et al.* A subpopulation of smooth muscle cells, derived from melanocyte-
834 competent precursors, prevents patent ductus arteriosus. *PloS One* **8**, e53183 (2013).
835 110. Goss, J. A. *et al.* Somatic mutations in intracranial arteriovenous malformations. *PloS*
836 *One* **14**, e0226852 (2019).
837 111. Zenner, K. *et al.* Somatic activating BRAF variants cause isolated lymphatic
838 malformations. *HGG Adv.* **3**, 100101 (2022).
839 112. Zeng, X. *et al.* The Coexistence of Gliosarcoma and Arteriovenous Malformation with the
840 BRAF V600E Mutation. *World Neurosurg.* **134**, 594–597 (2020).
841 113. Fultang, L. *et al.* Macrophage-Derived IL1β and TNFα Regulate Arginine Metabolism in
842 Neuroblastoma. *Cancer Res.* **79**, 611–624 (2019).
843 114. Bedoya-Reina, O. C. *et al.* Single-nuclei transcriptomes from human adrenal gland reveal
844 distinct cellular identities of low and high-risk neuroblastoma tumors. *Nat. Commun.* **12**,
845 5309 (2021).
846 115. Jansky, S. *et al.* Single-cell transcriptomic analyses provide insights into the
847 developmental origins of neuroblastoma. *Nat. Genet.* **53**, 683–693 (2021).
848 116. Boeva, V. *et al.* Heterogeneity of neuroblastoma cell identity defined by transcriptional
849 circuitries. *Nat. Genet.* **49**, 1408–1413 (2017).
850 117. Buttgereit, A. *et al.* Sall1 is a transcriptional regulator defining microglia identity and
851 function. *Nat. Immunol.* **17**, 1397–1406 (2016).
852 118. The World Medical Association, (WMA). WMA Declaration of Helsinki. *Ethical Principles*
853 *for Medical Research Involving Human Subjects* https://www.wma.net/policies-post/wma-
854 declaration-of-helsinki-ethical-principles-for-medical-research-involving-human-subjects/
855 (2022).

856 119. Journal Officiel, F. *LOI n° 2021-1017 du 2 août 2021 relative à la bioéthique*. (2021).
857 120. Feltri, M. L. *et al.* P0-Cre transgenic mice for inactivation of adhesion molecules in
858 Schwann cells. *Ann. N. Y. Acad. Sci.* **883**, 116–123 (1999).
859 121. Voiculescu, O., Charnay, P. & Schneider-Maunoury, S. Expression pattern of a Krox-
860 20/Cre knock-in allele in the developing hindbrain, bones, and peripheral nervous system.
861 *Genes. N. Y. N 2000* **26**, 123–126 (2000).
862 122. Ericson, J., Morton, S., Kawakami, A., Roelink, H. & Jessell, T. M. Two critical periods of
863 Sonic Hedgehog signaling required for the specification of motor neuron identity. *Cell* **87**,
864 661–673 (1996).
865 123. Dion, C. *et al.* SMCHD1 is involved in de novo methylation of the DUX4-encoding D4Z4
866 macrosatellite. *Nucleic Acids Res.* **47**, 2822–2839 (2019).
867 124. Blighe, K., Rana, S. & Lewis, M. Blighe K, Rana S, Lewis M (2023). EnhancedVolcano:
868 Publication-ready volcano plots with enhanced coloring and labeling. R package version
869 1.20.0. (2023).
870 125. Subramanian, A. *et al.* Gene set enrichment analysis: A knowledge-based approach for
871 interpreting genome-wide expression profiles. *Proc. Natl. Acad. Sci.* **102**, 15545–15550
872 (2005).
873 126. Kolberg, L. *et al.* g:Profiler—interoperable web service for functional enrichment analysis
874 and gene identifier mapping (2023 update). *Nucleic Acids Res.* **51**, W207–W212 (2023).
875 127. Evangelista, J. E. *et al.* Enrichr-KG: bridging enrichment analysis across multiple libraries.
876 *Nucleic Acids Res.* **51**, W168–W179 (2023).
877 128. Nusinow, D. P. *et al.* Quantitative Proteomics of the Cancer Cell Line Encyclopedia. *Cell*
878 **180**, 387-402.e16 (2020).
879 129. Grissa, D., Junge, A., Oprea, T. I. & Jensen, L. J. Diseases 2.0: a weekly updated
880 database of disease–gene associations from text mining and data integration. *Database*
881 **2022**, baac019 (2022).
882 130. Cao, J. *et al.* A human cell atlas of fetal gene expression. *Science* **370**, eaba7721 (2020).

883 131. Liao, Y., Wang, J., Jaehnig, E. J., Shi, Z. & Zhang, B. WebGestalt 2019: gene set analysis
884 toolkit with revamped UIs and APIs. *Nucleic Acids Res.* **47**, W199–W205 (2019).
885 132. Le, N. *et al.* Analysis of congenital hypomyelinating Egr2Lo/Lo nerves identifies Sox2 as
886 an inhibitor of Schwann cell differentiation and myelination. *Proc. Natl. Acad. Sci. U. S.*
887 *A.* **102**, 2596–2601 (2005).

888

889 # Figure legends

890 Figure 1. Constitutive MAPK activation mediated by a single copy of *Braf*^{V600E} in murine
891 Schwann cell progenitors induces early peripheral neuropathy and small body size.

892 **a)** By postnatal day (P)21, Mpz-*Braf* mice displayed abnormal hindlimb postural reflexes and
893 ability to keep hindfeet on the bars of a wire cage lid (arrowheads), indicating a functional
894 peripheral nerve defect. **b, c)** Western blot analysis of total and phosphorylated (p)Erk1/2
895 signaling performed on sciatic nerve lysates from **(b)** P5 and **(c)** P21 control and Mpz-*Braf*
896 mice. Gapdh was detected as a loading control. **d)** Protein densitometry in control (n=4) *vs*
897 mutant (n=5) sciatic nerve lysates at P5, and control (n=13) *vs* mutant (n=15) lysates at P21.
898 **e**) Body weight of both sexes was monitored at P5, P10, P21, P35 and P42 in control and Mpz-
899 *Braf* mice, respectively (n = 28 *vs* 8 at P5, n = 15 *vs* 5 at P10, n = 54 *vs* 45 at P21, n = 14 *vs*
900 10 at P35, n = 5 *vs* 5 at P42). **f**) Quantitative PCR analysis of *Ghr* and *Igf1* expression in control
901 (n=5) *vs* mutant (n=5) livers at P21. Statistical significance from unpaired Mann-Whitney test
902 in **d**), two-way ANOVA followed by Šidák's post-hoc test in **f**), and Student's t-test in **g**): ns, not
903 significant; * $p < 0.05$; ** $p < 0.01$; *** $p < 0.001$; **** $p < 0.0001$.

904 Figure 2. Myelination initiation is not impaired in *Braf*-mutant sciatic nerves, while
905 maintenance is compromised.

906 **a)** Macroscopic examination of control and mutant sciatic nerve at P5 and P21. Arrows indicate
907 Fontana bands, present only in control nerves. **b)** Sciatic nerve diameter measurements at P5,
908 P10, P21, and P35 in both Mpz-*Braf* and control mice (n = 11 *vs* 6 at P5, n = 6 *vs* 4 at P10, n
909 = 15 *vs* 10 at P21, and n = 5 *vs* 5 at P35; in control *vs* mutant nerves, respectively). Two-way
910 ANOVA followed by Šidák's post-hoc test; ns, not significant; ** $p < 0.01$; **** $p < 0.0001$. **c)**
911 Representative transmission electron micrographs of sciatic nerve cross-sections at P5 and
912 P21 from control and mutant mice. Bars = 10 µm except for magnified axons at P28, 2 µm.
913 Arrows, myelin aberrations; c, extracellular collagen; f, fibroblast; nm, non-myelinating
914 Schwann cell; sc, myelinating Schwann cell;.

915 Figure 3. Braf^{V600E} in Schwann cells triggers demyelination and degeneration of large-
916 caliber axons

917 **a)** Mean axon diameter at P5 (n = 3 per genotype, not significantly [ns] different). **b**)
918 MyelTracer-obtained *g*-ratios as a function of axon diameter at P5, to assess myelin thickness
919 in control (n = 803) *vs* mutant (n=811) myelinated fibers (n=3 per genotype). The slopes of a
920 simple linear regression do not vary significantly across P5 genotypes. **c)** Axon density
921 decreases physiologically between P21 and P28 in control sciatic nerves but is significantly
922 reduced to 7-11% of normal levels in mutant nerves at these stages. **d**) Mean axon diameter
923 per genotype at P28 (n = 2 per genotype) shows that smaller fibers remain on average. **d)**

924 Binning analysis of *g*-ratios as a function of axon diameter at P28. A total of n = 792 *vs* 746
925 myelinated axons were analyzed for control *vs* mutant nerves, respectively, from 2 individuals
926 of each group (correlation significance indicated by asterisks). **f)** *g*-ratios of axonal diameters
927 at P28, with a significantly different slope (p<0.0001) after simple linear regression, where
928 mutant *g*-ratios increase most with size. **g**) When binned by diameter ranges (small 0-1 µm,
929 medium 1-3 µm, and large >3 µm), there is modestly significant hypermyelination in small
930 axons but more significant hypomyelination at diameters over 1 µm. Statistical significance
931 was assessed with two-way ANOVA followed by Šidák's post-hoc test; ns, not significant; * p
932 < 0.05; ** p < 0.01; *** p < 0.001; **** p < 0.0001.

933 Figure 4. Segmental demyelination is preceded by myelin disassembly in Mpz-*Braf* mice.

934 Teased fibers from sciatic nerves of control (**a, e**) and Mpz-*Braf* mice (**b-d**, **f-g**) at P5 (top
935 panels) and P21 (bottom panels) were immunostained with antibodies against Mbp and Caspr
936 and Alexa Fluor-488-conjugated phalloidin. Mpz-*Braf* fibers had degenerating myelin ovoids
937 (white arrowheads), fewer apparent nodes of Ranvier with diffusing paranodal Caspr (orange
938 arrowheads), and segmental demyelination, not observed in controls. Nuclear DNA was
939 stained with DAPI (grey). Maximum intensity z-projection images were generated in **b, e** and **f**
940 with Nikon NIS-Elements Viewer software. Scale bars: 50 µm (**a, b, f**) or 10 µm (**c, e, g**).

941 Figure 5. Comparative transcriptomics show downregulation of myelin sheath
942 component transcripts in *Braf*-mutant sciatic nerves.

943 **a)** RNA-seq analysis was performed in control and Mpz-*Braf* mutant sciatic nerves (n = 4 per
944 genotype). Volcano plots depict the DEGs in *Braf*-mutant sciatic nerves relative to controls at
945 P5 (left panel) and P21 (right panel). An adjusted *p*-value < 0.5 and Log2FC <-1 (blue) or >1
946 (red) were used as thresholds to define DEGs. The top 15 DEGs are labeled on each graph
947 according to Manhattan distance. **b)** Volcano plots illustrate the differentially enriched
948 pathways provided by GSEA through WebGestalt https://www.webgestalt.org/ [131] using the
949 mouse Wikipathway database. Pathways are significantly enriched when false discovery rate
950 (FDR) < 0.05 and normalized enrichment score (NES) < -1 (blue) or >1 (red). Circle diameter
951 is proportional to gene ratio (count of core enrichment genes / count of pathway genes). **c)**
952 Enrichment plot for "cholesterol biosynthesis", the most significant gene set downregulated in
953 mutant sciatic nerves (p-value and FDR < 0.001, NES = -2.3). **d)** Dot plot displaying log2 fold-
954 change (Log2FC) of myelin-associated genes (*Mpz*, *Pmp22*, and *Mbp* in bold, representing
955 transcripts of the primary myelin sheath proteins).

956 Figure 6. *Egr2* and its target genes decrease in Mpz-*Braf* nerves with concomitant
957 increase in expression of negative regulators of myelination

958 **a)** Dot plot displaying log2 fold-change (Log2FC) of known positive (*Sox10*, *Egr2*) or negative
959 (*Jun*, *Sox2*) transcriptional regulators of myelination in RNAseq of mutant *vs* control sciatic
960 nerves at P5 and P21. **b)** Western blot of Jun and Egr2 in sciatic nerve lysates from P21 and
961 P42 Mpz-*Braf* and control mice. Gapdh was detected as a loading control. N=13 individuals of
962 each genotype. Statistical significance was assessed by an unpaired Mann-Whitney test; ns,
963 not significant; ** $p < 0.01$; *** $p < 0.001$; **** $p < 0.0001$. **c)** Enrichment plot for up- or down-
964 regulated genes (top and bottom panels, respectively) showing that most genes are commonly
965 deregulated in sciatic nerves from either the *Mpz-Braf* or homozygous *Egr2* hypomorphic allele
966 mice [132]. **d-e)** Spearman's *rho* to assess significance of correlation was calculated from bulk
967 RNAseq of Mpz-*Braf* sciatic nerves at P5 (top panels) or P21 (bottom panels), with analogous
968 datasets at P8 and P30 from Egr2-*Cre*-driven (**d**) overexpression of constitutively active Mek1
969 (Egr2-*Cre*; *Mek1*DD) or (**e**) knockout of *Shp2* (Egr2-*Cre*; *Shp2*$^{f/f}$).

970 Figure 7. Activation of injury-related genes in Mpz-*Braf* sciatic nerves.

971 **a**) GSEA analysis of upregulated genes at P21 shows highly significant correlation with the
972 Wikipathway annotation "Spinal cord injury" (WP2431). **b**) These are also significantly and
973 positively correlated with genes upregulated in regenerating nerves of young adult mice 7 days
974 after axotomy. **c**) Transcription of *Shh*, *Gdnf* and *Nrg1* are greatly increased at both P5 and
975 P21, while Gdnf-family member *Artn* and *Nrg1* receptor ErbB3 are only significantly
976 upregulated at P21. Teased fibers from sciatic nerves of P21 control and Mpz-*Braf* mice
977 immunostained against (**d**) S100b (yellow) and Shh (magenta), with DAPI nuclear counterstain
978 (gray), or (**f**) Pmp2 (orange) and Erbb3 (blue). Scale bars: 50 µm (**d**) or 10 µm **(f**).

979 Figure 8. Patient-derived immature Schwann cells express inappropriate gene
980 signatures *in vitro*.

981 **a)** Summary of hiPSC-directed differentiation into SC, derived from two unrelated WT (HFF15
982 shown here and AG08H) and from unrelated adolescent girls, both carrying the *BRAF* p.Q257R
983 variant (CFC patients RMK0056C, RMK0138C) over time. Representative bright-field images
984 shown at D13, D19, a day after passage on D32, and at D95-100. Scale bar = 100 µm for all
985 frames. **b**) Euler diagram showing the number of common/specific dysregulated genes (*p*-
986 value < 0.05, Log2FC > 1 or < -1) in RMK0056C and RMK0138C mutant cells compared to
987 control cells (HFF15) at D21 of differentiation. (C) Bubble plot of enrichment analysis of the
988 common 380 dysregulated genes in RMK0056C and RMK0138C. Gene set names from the
989 REACTOME database are indicated on the y-axis. Gene sets are ranked according to
990 significance level (-log adjusted p-value). The size of the dots represents the number of queried

991 genes present in the corresponding pathway, and the color corresponds to the gene ratio
992 (number of queried genes present in the gene set / gene set size). (D) Enrichment plot for
993 Egr2- and Sox10-mediated initiation of SC myelination using Reactome database,
994 corresponding to the significant gene set downregulated in RMK0056C and RMK0138C cell
995 lines after 30 days of differentiation. (E) Enrichr-KG analysis of the most significantly enriched
996 terms across three additional databases (Descartes Cell Types and Tissue 2021, Jensen
997 DISEASES and CCLE Proteomics 2020) highlight the close lineage relationship between
998 Schwann cell progenitors and either melanocytes (“melanoma” and “skin cancer”, the A2058
999 cell line) or neuroendocrine cells (“visceral neurons in lung/heart”, the SKNAS and NCIH446
1000 cell lines).

Figure 1

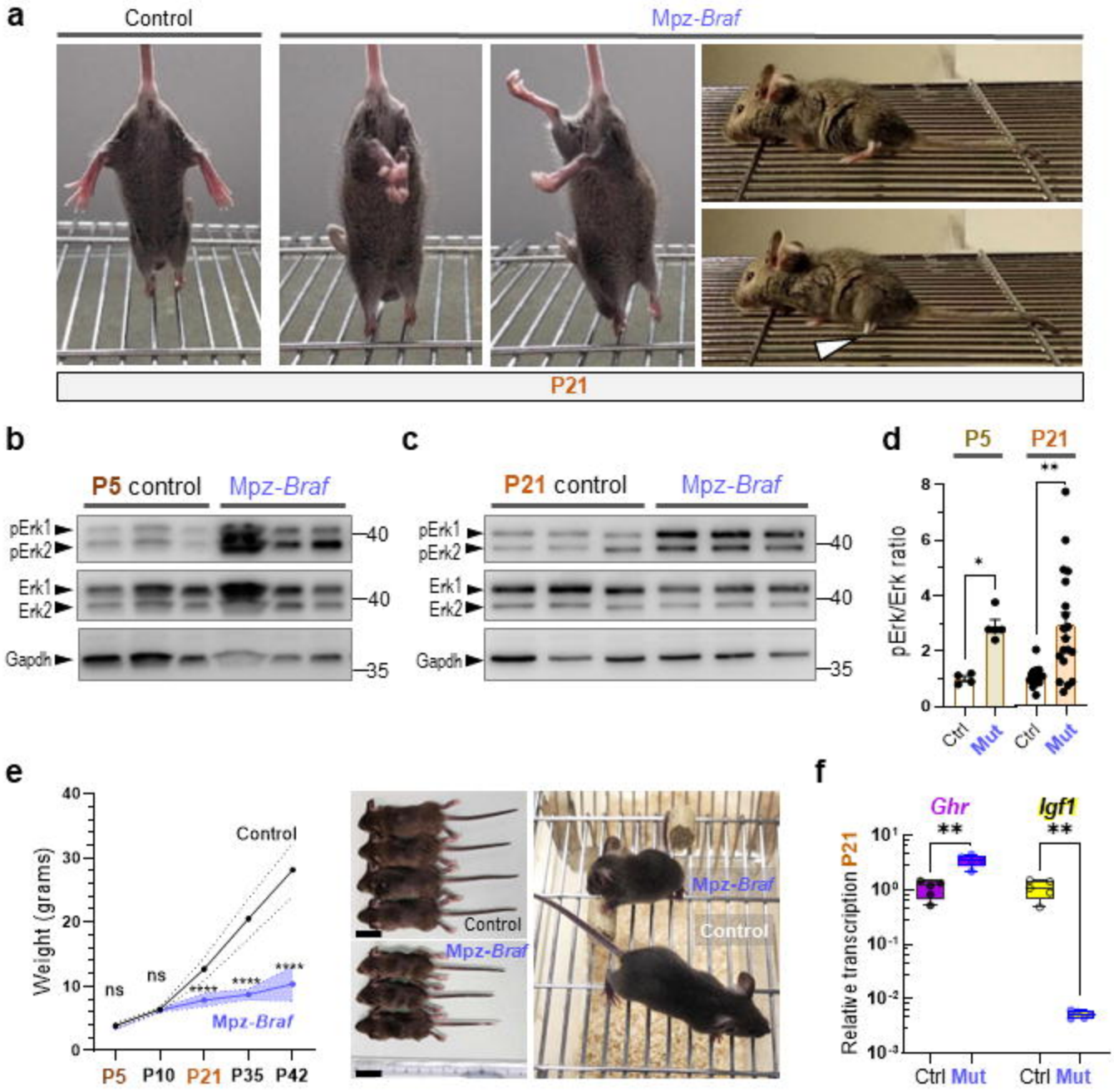
a
Control
Mpz-Braf
P21
b
P5 control
Mpz-Braf
pErk1
pErk2
Erk1
Erk2
Gapdh
40
40
35
c
P21 control
Mpz-Braf
pErk1
pErk2
Erk1
Erk2
Gapdh
40
40
35
d
P5
P21
pErk/Erk ratio
Ctrl
Mut
Ctrl
Mut
e
Weight (grams)
Control
Mpz-Braf
ns
ns
****
****
****
P5
P10
P21
P35
P42
Control
Mpz-Braf
Mpz-Braf
Control
f
Ghr
Igf1
Relative transcription P21
**
**
Ctrl
Mut
Ctrl
Mut

Figure 2

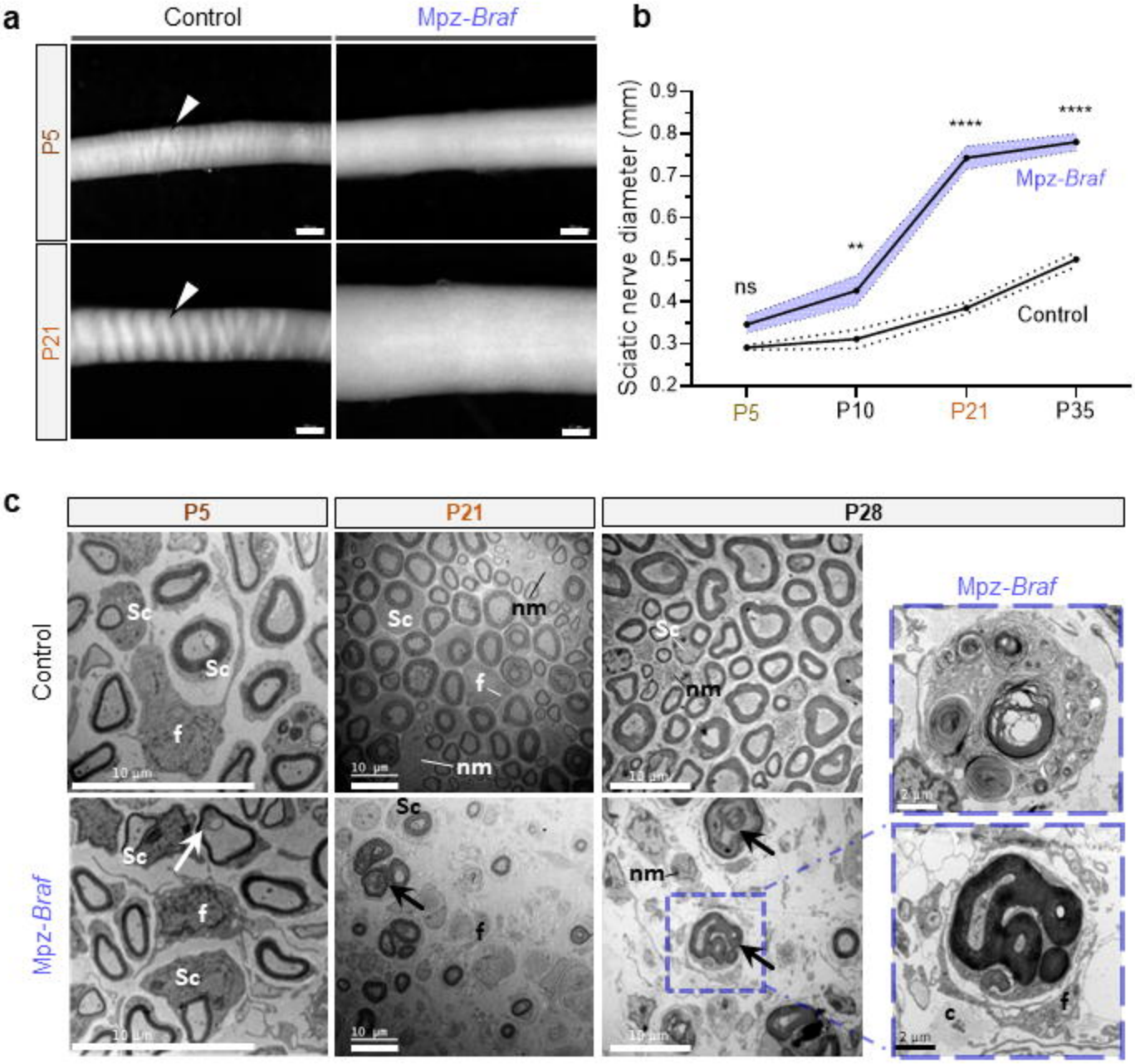
a
Control
Mpz-Braf
P5
P21
b
Sciatic nerve diameter (mm)
0.9
0.8
0.7
0.6
0.5
0.4
0.3
0.2
ns
**
****
****
Mpz-Braf
Control
P5
P10
P21
P35
c
P5
P21
P28
Control
Mpz-Braf
Sc
f
nm
c
10 µm
2 µm

Figure 3

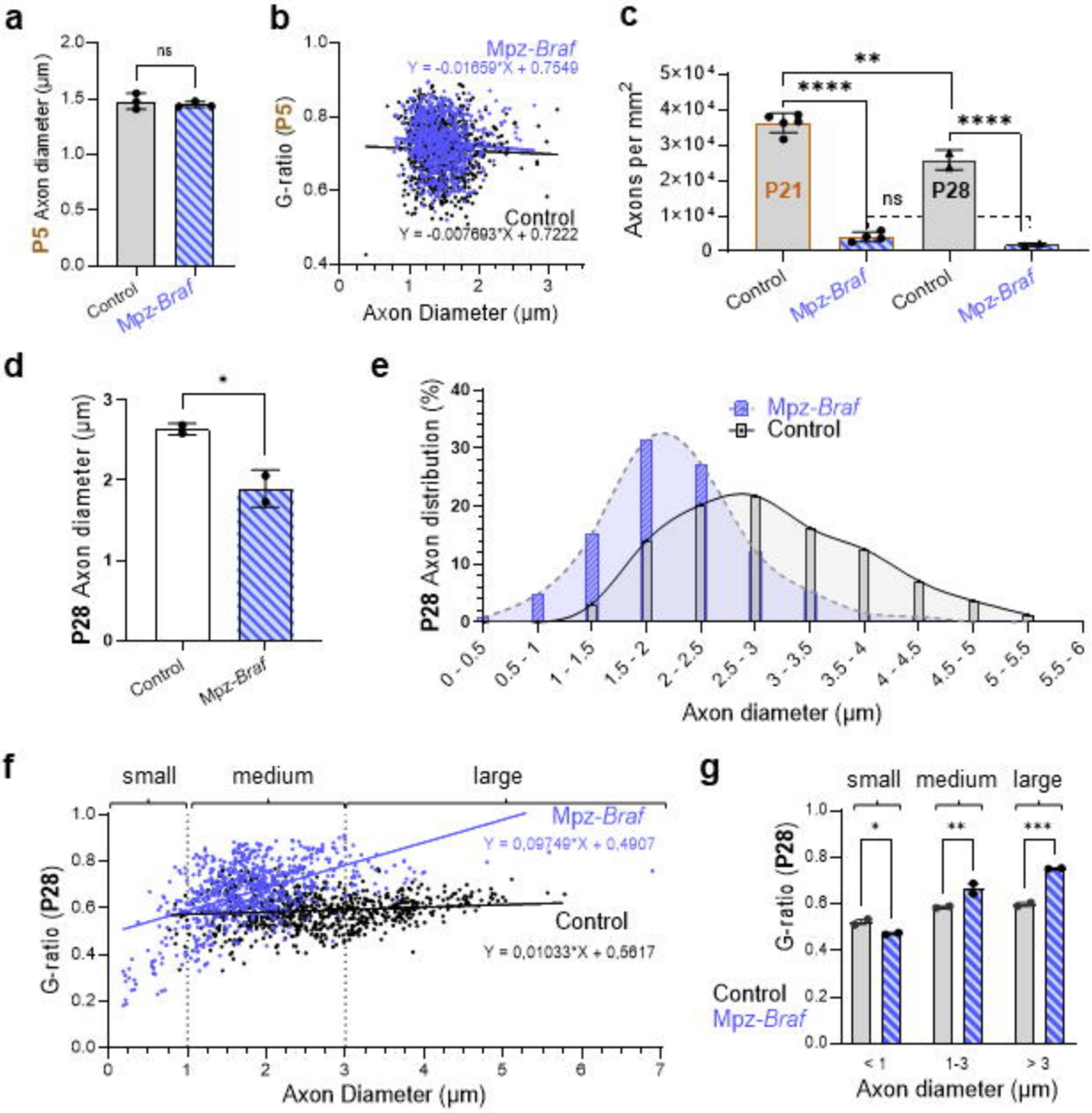
a
P5 Axon diameter (µm)
ns
Control
Mpz-Braf
b
G-ratio (P5)
Mpz-Braf
Y = -0.01659*X + 0.7549
Control
Y = -0.007693*X + 0.7222
Axon Diameter (µm)
c
Axons per mm²
P21
P28
ns
Control
Mpz-Braf
Control
Mpz-Braf
d
P28 Axon diameter (µm)
Control
Mpz-Braf
e
P28 Axon distribution (%)
Mpz-Braf
Control
Axon diameter (µm)
f
small
medium
large
G-ratio (P28)
Mpz-Braf
Y = 0,09749*X + 0,4907
Control
Y = 0,01033*X + 0,5617
Axon Diameter (µm)
g
small
medium
large
G-ratio (P28)
Control
Mpz-Braf
< 1
1-3
> 3
Axon diameter (µm)

Figure 4

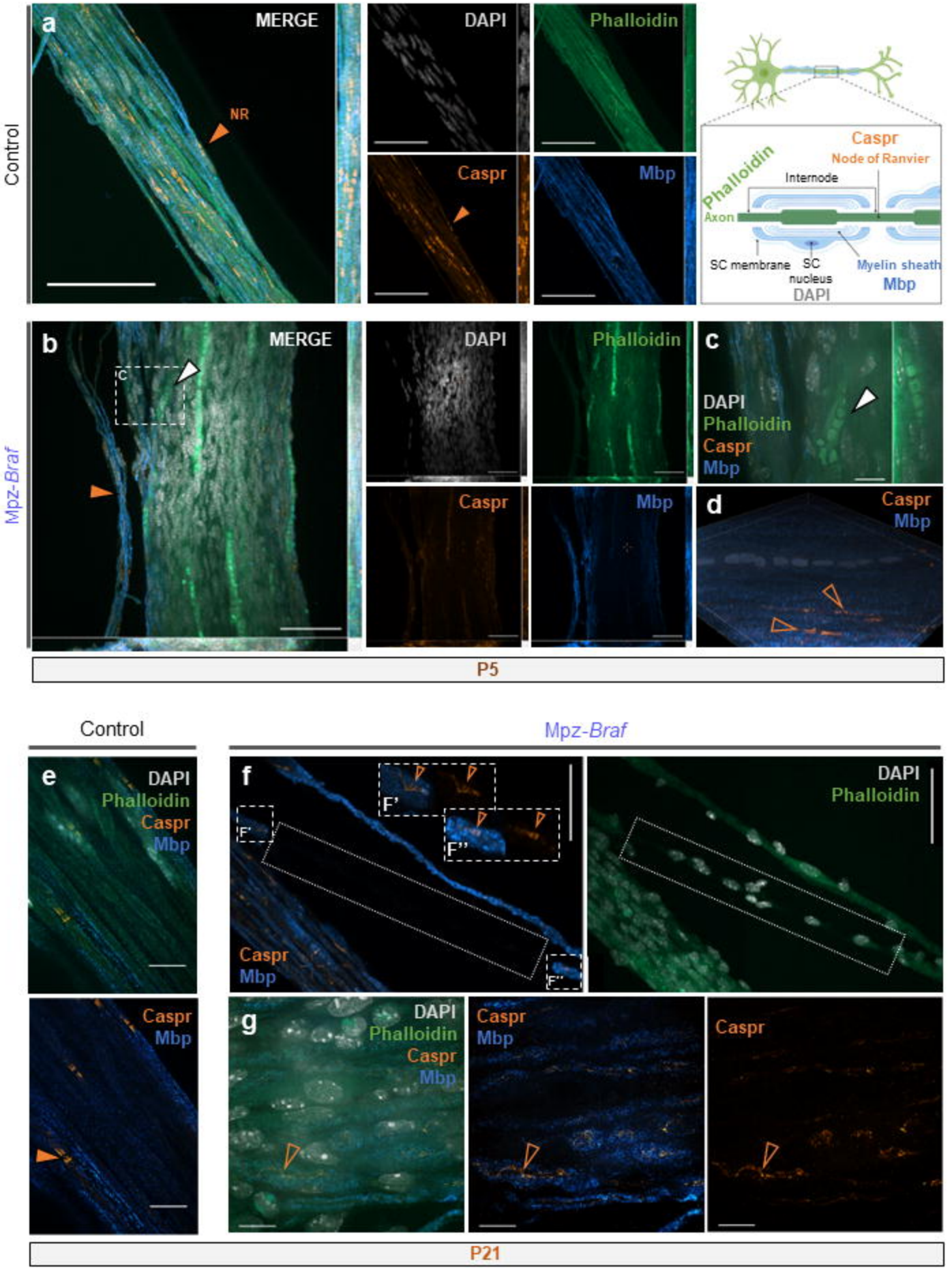
a
MERGE
NR
DAPI
Phalloidin
Caspr
Mbp
Control
Caspr
Node of Ranvier
Internode
Phalloidin
Axon
SC membrane
SC nucleus
DAPI
Myelin sheath
Mbp
b
MERGE
c
DAPI
Phalloidin
Caspr
Mbp
Mpz-Braf
d
Caspr
Mbp
P5
Control
Mpz-Braf
e
DAPI
Phalloidin
Caspr
Mbp
f
F'
F''
Caspr
Mbp
DAPI
Phalloidin
g
DAPI
Phalloidin
Caspr
Mbp
Caspr
Mbp
Caspr
P21

Figure 5

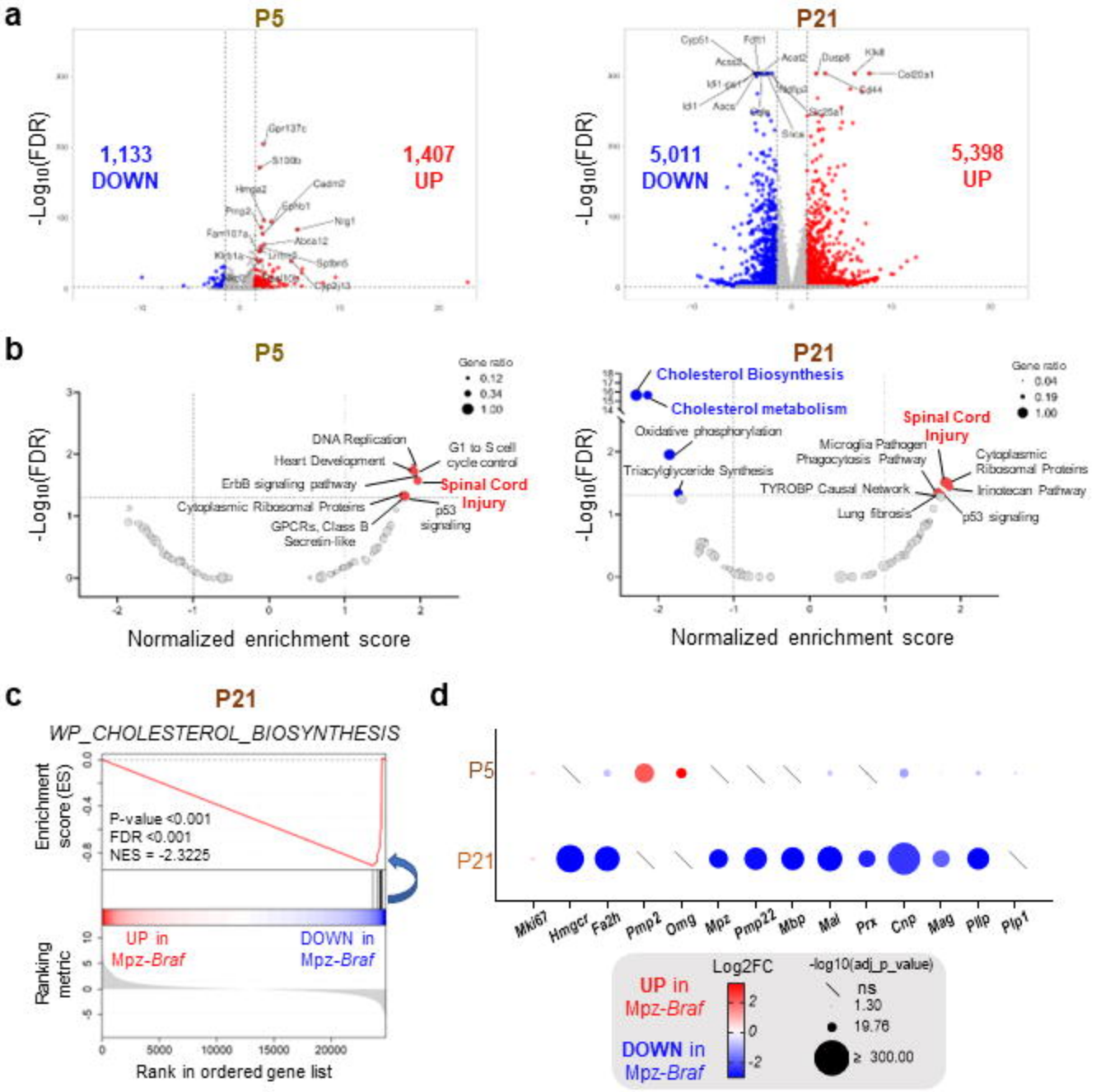
a
P5
1,133
DOWN
1,407
UP
-Log10(FDR)
P21
5,011
DOWN
5,398
UP
b
P5
Gene ratio
0.12
0.34
1.00
DNA Replication
Heart Development
G1 to S cell cycle control
ErbB signaling pathway
Spinal Cord Injury
Cytoplasmic Ribosomal Proteins
p53 signaling
GPCRs, Class B Secretin-like
Normalized enrichment score
P21
Cholesterol Biosynthesis
Cholesterol metabolism
Oxidative phosphorylation
Triacylglyceride Synthesis
Spinal Cord Injury
Microglia Pathogen Phagocytosis Pathway
Cytoplasmic Ribosomal Proteins
TYROBP Causal Network
Irinotecan Pathway
Lung fibrosis
p53 signaling
c
P21
WP_CHOLESTEROL_BIOSYNTHESIS
Enrichment score (ES)
P-value <0.001
FDR <0.001
NES = -2.3225
Ranking metric
UP in Mpz-Braf
DOWN in Mpz-Braf
Rank in ordered gene list
d
P5
P21
Mki67
Hmgcr
Fa2h
Pmp2
Omg
Mpz
Pmp22
Mbp
Mal
Prx
Cnp
Mag
Plp
Plp1
Log2FC
-log10(adj_p_value)
ns
1.30
19.76
≥ 300.00
UP in Mpz-Braf
DOWN in Mpz-Braf

Figure 6

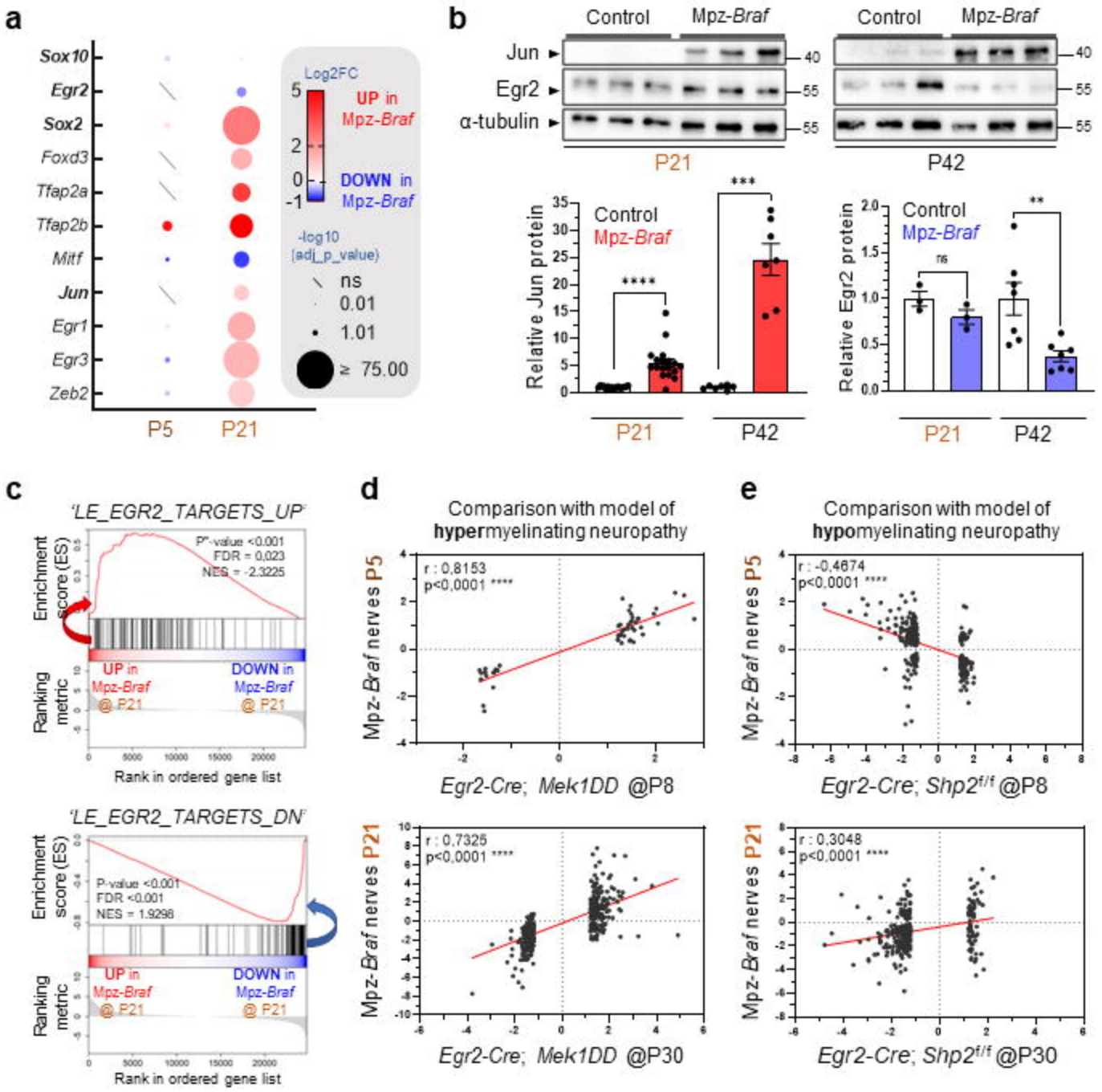
a
Sox10
Egr2
Sox2
Foxd3
Tfap2a
Tfap2b
Mitf
Jun
Egr1
Egr3
Zeb2
P5
P21
Log2FC
UP in Mpz-Braf
DOWN in Mpz-Braf
-log10 (adj_p_value)
ns
0.01
1.01
≥ 75.00
b
Control
Mpz-Braf
Jun
Egr2
α-tubulin
P21
P42
Relative Jun protein
Relative Egr2 protein
c
'LE_EGR2_TARGETS_UP'
Enrichment score (ES)
P-value <0.001
FDR = 0,023
NES = -2.3225
Ranking metric
UP in Mpz-Braf @ P21
DOWN in Mpz-Braf @ P21
Rank in ordered gene list
'LE_EGR2_TARGETS_DN'
P-value <0.001
FDR <0.001
NES = 1.9298
d
Comparison with model of hypermyelinating neuropathy
Mpz-Braf nerves P5
r : 0,8153
p<0,0001 ****
Egr2-Cre; Mek1DD @P8
Mpz-Braf nerves P21
r : 0,7325
p<0,0001 ****
Egr2-Cre; Mek1DD @P30
e
Comparison with model of hypomyelinating neuropathy
r : -0,4674
p<0,0001 ****
Egr2-Cre; Shp2f/f @P8
r : 0,3048
p<0,0001 ****
Egr2-Cre; Shp2f/f @P30

Figure 7

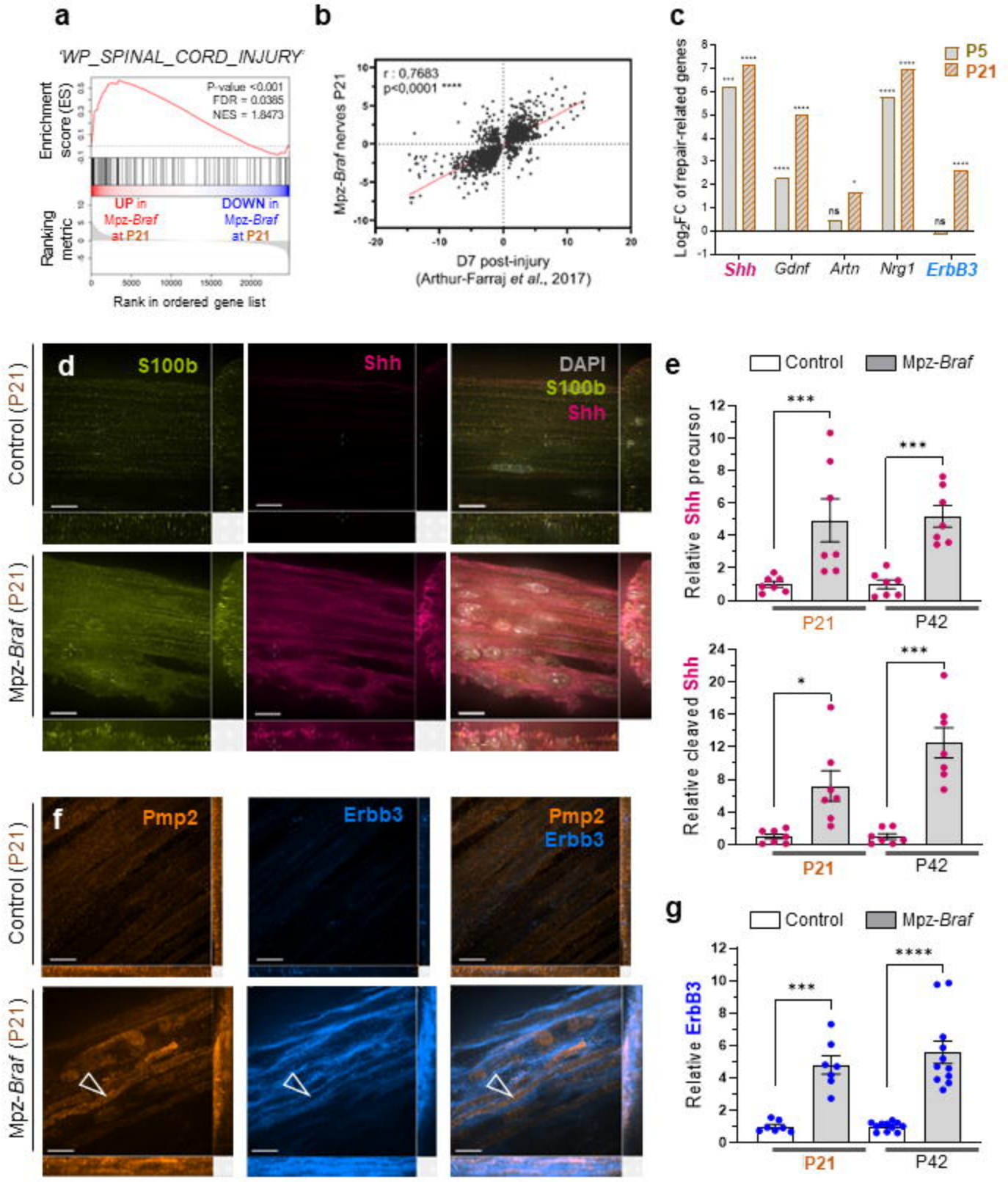
a
'WP_SPINAL_CORD_INJURY'
Enrichment score (ES)
P-value <0.001
FDR = 0.0385
NES = 1.8473
Ranking metric
UP in Mpz-Braf at P21
DOWN in Mpz-Braf at P21
Rank in ordered gene list
b
r : 0,7683
p<0,0001 ****
Mpz-Braf nerves P21
D7 post-injury
(Arthur-Farraj et al., 2017)
c
P5
P21
Log2FC of repair-related genes
Shh
Gdnf
Artn
Nrg1
ErbB3
d
S100b
Shh
DAPI
S100b
Shh
Control (P21)
Mpz-Braf (P21)
e
Control
Mpz-Braf
Relative Shh precursor
Relative cleaved Shh
P21
P42
f
Pmp2
Erbb3
Pmp2
Erbb3
Control (P21)
Mpz-Braf (P21)
g
Control
Mpz-Braf
Relative ErbB3
P21
P42

Figure 8

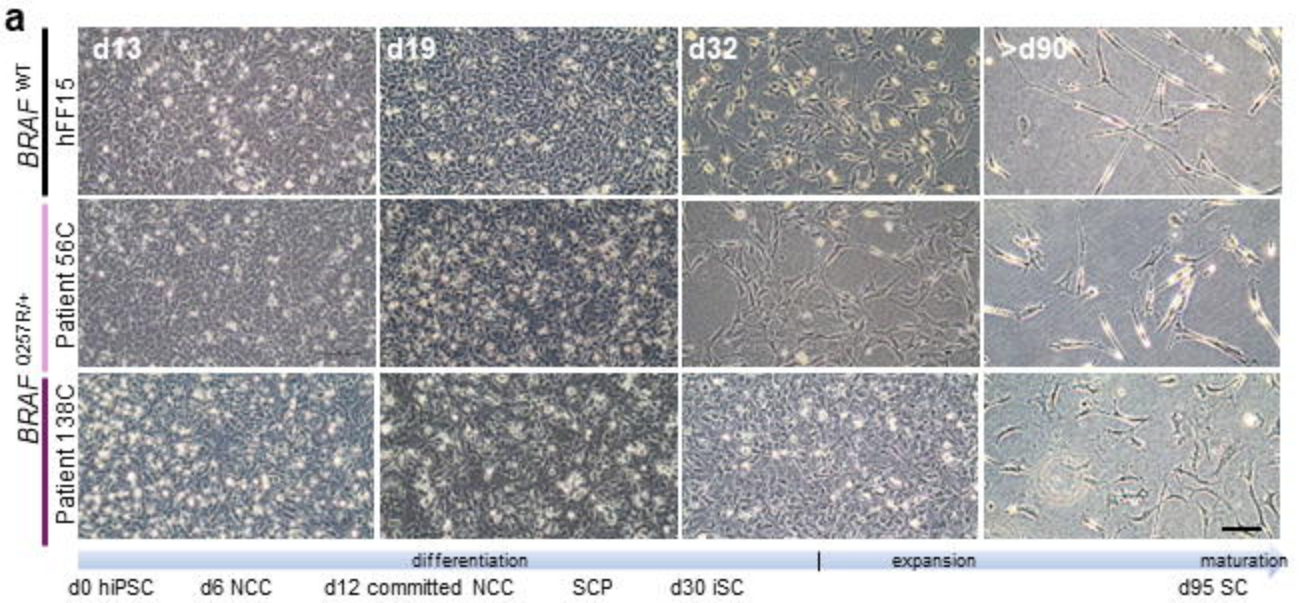
a
d13
d19
d32
>d90
BRAF WT
hFF15
BRAF Q257R/+
Patient 56C
Patient 138C
differentiation
expansion
maturation
d0 hiPSC
d6 NCC
d12 committed NCC
SCP
d30 iSC
d95 SC

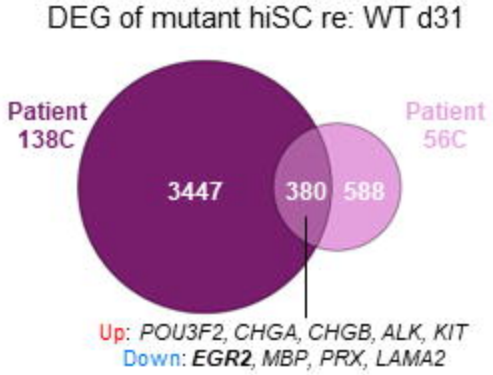
b
DEG of mutant hiSC re: WT d31
Patient 138C
Patient 56C
3447
380
588
Up: POU3F2, CHGA, CHGB, ALK, KIT
Down: EGR2, MBP, PRX, LAMA2

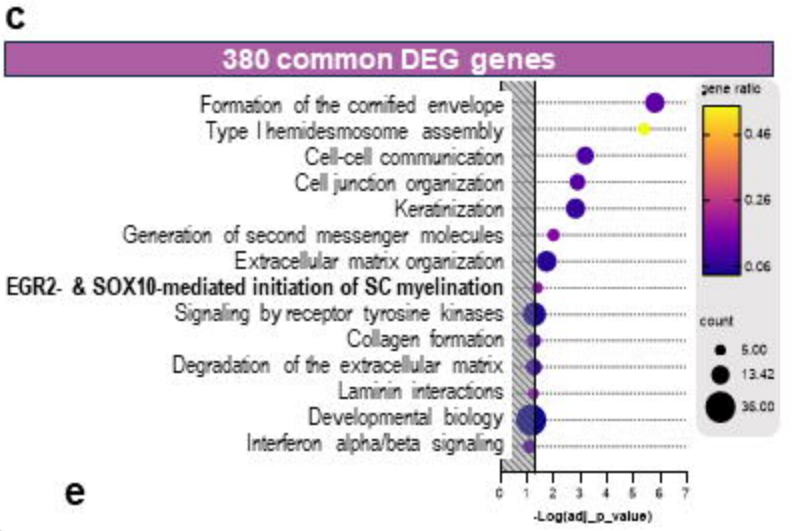
c
380 common DEG genes
Formation of the cornified envelope
Type I hemidesmosome assembly
Cell-cell communication
Cell junction organization
Keratinization
Generation of second messenger molecules
Extracellular matrix organization
EGR2- & SOX10-mediated initiation of SC myelination
Signaling by receptor tyrosine kinases
Collagen formation
Degradation of the extracellular matrix
Laminin interactions
Developmental biology
Interferon alpha/beta signaling
gene ratio
0.46
0.26
0.06
count
5.00
13.42
36.00
0 1 2 3 4 5 6 7
-Log(adj_p_value)

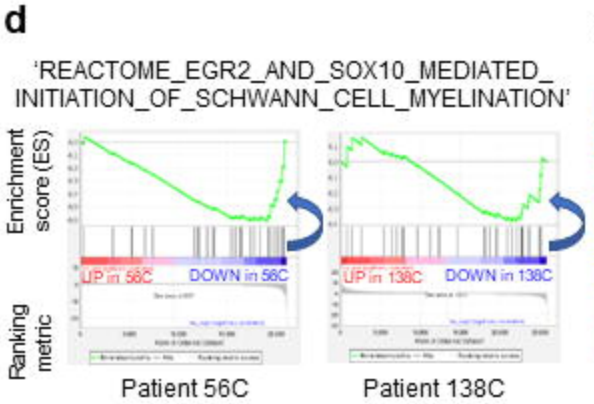
d
'REACTOME_EGR2_AND_SOX10_MEDIATED_INITIATION_OF_SCHWANN_CELL_MYELINATION'
Enrichment score (ES)
Ranking metric
UP in 56C
DOWN in 56C
UP in 138C
DOWN in 138C
Patient 56C
Patient 138C

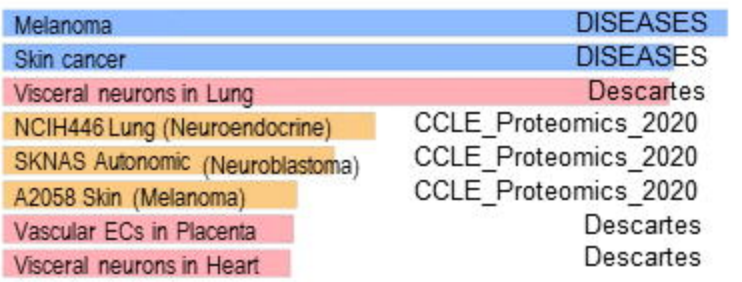
e
Melanoma DISEASES
Skin cancer DISEASES
Visceral neurons in Lung Descartes
NCIH446 Lung (Neuroendocrine) CCLE_Proteomics_2020
SKNAS Autonomic (Neuroblastoma) CCLE_Proteomics_2020
A2058 Skin (Melanoma) CCLE_Proteomics_2020
Vascular ECs in Placenta Descartes
Visceral neurons in Heart Descartes